

The Cosmological Trajectories Method: Modelling cosmic structure formation in the non-linear regime

F. C. Lane,^{1*} A. N. Taylor,^{1†} and D. Sorini^{1‡}

¹*Scottish Universities Physics Alliance, Institute for Astronomy, School of Physics and Astronomy, University of Edinburgh, Royal Observatory, Blackford Hill, Edinburgh, EH9 3HJ, U.K.*

Accepted XXX. Received YYY; in original form ZZZ

ABSTRACT

We introduce a novel approach, the Cosmological Trajectories Method (CTM), to model nonlinear structure formation in the Universe by expanding gravitationally-induced particle trajectories around the Zel’dovich approximation. A new Beyond Zel’dovich approximation is presented, which expands the CTM to leading second-order in the gravitational interaction and allows for post-Born gravitational scattering. In the Beyond Zel’dovich approximation we derive the exact expression for the matter clustering power spectrum. This is calculated to leading order and is available in the CTM MODULE. We compare the Beyond Zel’dovich approximation power spectrum and correlation function to other methods including 1-loop Standard Perturbation Theory (SPT), 1-loop Lagrangian Perturbation Theory (LPT), and Convolution Lagrangian Perturbation Theory (CLPT). We find that the Beyond Zel’dovich approximation power spectrum performs well, matching simulations to within $\pm 10\%$, on mildly non-linear scales, and at redshifts above $z = 1$ it outperforms the Zel’dovich approximation. We also find that the Beyond Zel’dovich approximation models the BAO peak in the correlation function at $z = 0$ more accurately, to within $\pm 5\%$ of simulations, than the Zel’dovich approximation, SPT 1-loop and CLPT.

Key words: Cosmology – methods: data analysis, statistical – cosmological parameters – large-scale structure of Universe

1 INTRODUCTION

Deciphering how the cosmic web and large-scale structure is formed in our Universe is an essential part of understanding cosmology. Better knowledge of large-scale structure formation will allow us to extract more information from current (e.g. [Planck Collaboration et al. 2020](#), [Hildebrandt et al. 2017](#), [Abbott et al. 2018](#)) and future observations of our Universe. Gathering more statistical information from current and upcoming surveys such as the Dark Energy Spectroscopic Instrument ([Levi et al. 2019](#)), the Vera Rubin Observatory ([LSST Science Collaboration et al. 2009](#)) and *Euclid* ([Racca et al. 2016](#)) will lead to tighter constraints on viable cosmological, gravity and structure formation models.

Modelling the cosmic web involves knowing how structures form under the influence of gravity. In the first approximation, the equations governing the evolution of density perturbations can be linearised. While this approach is accurate enough to describe the large-scale modes, it inevitably breaks down on small scales, where the local density field can become much larger than the average background density of the Universe. The breakdown of linear theory was found to occur around Fourier modes with wavenumber $k > 0.1 \text{ h Mpc}^{-1}$ ([Sugiyama 2014](#), [McQuinn & White 2016](#)), hence this regime is generally referred to as “non-linear regime”. A further degree of complexity comes into play when considering the impact of baryonic effects on galactic scales, such as winds ejected due to

supernovae explosions or jets from active galactic nuclei (see e.g. [Somerville & Davé 2015](#), for a review).

Because of the non-linear and interconnected nature of the physical processes driving structure formation, the current preferred method for investigating structure formation in the non-linear regime is to run large cosmological simulations. N-body (dark matter only) and hydrodynamic (dark matter and baryons) simulations can be used to simulate the gravitational evolution of structure in the Universe. One of the first large N-body simulations, the Millennium simulation ([Springel et al. 2005](#)), modelled the evolution of around a million dark matter particles from $z = 127$ to $z = 0$. Recent hydrodynamic simulations such as EAGLE ([Crain et al. 2015](#), [Schaye et al. 2015](#)), Illustris-TNG ([Weinberger et al. 2017](#), [Pillepich et al. 2018](#)), the New Horizon runs ([Kim et al. 2011](#), [Dubois et al. 2020](#)) and Simba ([Davé et al. 2019](#)) have furthered our understanding of structure formation and baryonic effects.

The large volume and high precision of data from forthcoming surveys demands at least comparable accuracy in theoretical models of structure formation. For this reason, simulations would need to probe a wide range of scales, while retaining high enough resolution to properly capture small-scale physics. However, the consequent computational cost in terms of memory and computer time hinders the exploration of a wide parameter space. This represents an issue when testing multiple theories of gravity and cosmological models, which typically requires obtaining predictions for several choices of the underlying parameters. Thus, there is clearly an interest for searching alternative and less costly methods.

Cosmological emulators provide a way of predicting the non-linear growth of structure for a range of cosmological parameters

* E-mail: flane@roe.ac.uk

† E-mail: ant@roe.ac.uk

‡ E-mail: sorini@roe.ac.uk

and some modified gravity theories. Emulators are generally trained on large sets of high-resolution simulation runs but once they have been trained on the simulation output they can be made publicly available for the community to utilise. In this paper, we will utilise the EUCLID EMULATOR (Knabenhans et al. 2019) which was developed for the *Euclid* space telescope and was trained on a sample of 100 input runs of PKDGRAV3 (Stadel et al. 2002, Potter et al. 2017). Other examples of emulators include COSMICEMU (Heitmann et al. 2010, 2009, Lawrence et al. 2010, Heitmann et al. 2013, Lawrence et al. 2017) trained on the Coyote Universe simulations, MGEMU (Ramachandra et al. 2020) an emulator that can model the ratio between the Λ -CDM power spectrum and the Hu-Sawicki $f(R)$ gravity (Hu & Sawicki 2007) power spectrum, the AEMULUS (DeRose et al. 2019) project and the DARK QUEST (Nishimichi et al. 2019) project. Although both simulations and emulators allow us to probe the non-linear regime accurately, analytic techniques can allow us to see how density field correlations arise more easily.

One technique that does not require the running of simulations and can give a more in-depth insight into structure formation is perturbation theory. Standard Perturbation Theory (SPT) or Eulerian Perturbation Theory (EPT) can reproduce cosmological observations up to scales of around $k \sim 0.1 \text{ h Mpc}^{-1}$, where non-linear gravitational and baryonic effects become important (Peebles 1980, Bertschinger 1995, Bouchet 1996, Bernardeau et al. 2002, Carlson et al. 2009, Bernardeau 2013). SPT can be extended to model smaller scales using IR-resummation (accounting for the physical effects of bulk flows) and loop corrections (next to leading order corrections), as demonstrated in Crocce & Scoccimarro (2006a,b), Taruya & Hiramoto (2008), Bernardeau et al. (2008, 2012, 2014) and Blas et al. (2014). Lagrangian Perturbation Theory (LPT) is another technique that can be used to model the formation of structure (Moutarde et al. 1991, Catelan 1995, Buchert 1992, Buchert & Ehlers 1993, Bouchet 1996, Tatekawa 2004, Rampf & Buchert 2012). LPT, unlike SPT, follows the motion of particles through a system and has been found to be more accurate at equal orders than SPT (Matsubara 2008a,b, Bouchet et al. 1995, Carlson et al. 2013, White 2014, Catelan 1995).

The Zel'dovich approximation (Zel'dovich 1970, Taylor 1993, Schneider & Bartelmann 1995, Taylor & Hamilton 1996, White 2014), a first-order LPT, is unique in that in 1D it is exact up until shell-crossing (the point at which streams of matter from different directions intersect) occurs. In 3D it behaves competitively with EPT and higher-order LPT. It is an intuitive method for describing how particles form the structures we see in the cosmic web (McQuinn & White 2016).

As discussed in McQuinn & White (2016), although techniques that aim to address the breakdown of perturbation theory on small scales have made an improvement (matching simulations up to $k = 0.2 \text{ h Mpc}^{-1}$ as discussed in Sugiyama 2014), fundamental failings on these scales remain. For example, it is well known that when the overdensity field becomes large ($\delta \gg 1$) these schemes are no longer valid. As mentioned above, both EPT and LPT also breakdown after shell-crossing occurs. However, we know that virialised structures in our Universe, such as dark matter haloes, are formed after shell-crossing occurs.

The Effective Field Theory of Large Scale Structure (EFTofLSS) is a method that aims to fix these issues by integrating out small wavelengths (Carrasco et al. 2012, 2014a,b, Carroll et al. 2014, Porto et al. 2014, Senatore & Zaldarriaga 2015, Vlah et al. 2015a,b, 2016a,b), to reduce the uncontrolled small-scale perturbative effects affecting large scales. EFTofLSS generally requires either data from simulations or observations to fix free parameters in the theory. Other methods for extending perturbation theory into the non-linear regime

including semi-classical propagators and methods based on field theory have been suggested in Seljak & Vlah (2015), Taruya & Colombi (2017), McDonald & Vlah (2018), Friedrich & Prokopec (2017), Friedrich & Prokopec (2018), Uhlemann et al. (2019), Friedrich & Prokopec (2019) and Halle et al. (2020).

A statistical mechanics approach to modelling gravitational interaction into the non-linear regime was introduced in Bartelmann et al. (2014a) and further developed in subsequent works (Bartelmann et al. 2014b, Fabis et al. 2014, Kozlikin et al. 2014, Viermann et al. 2015, Bartelmann et al. 2017, Sorini 2017, Lilow et al. 2019, Bartelmann et al. 2019). This theory is called Kinetic Field Theory (KFT). The theory was re-derived using particle trajectories in Ali-Haïmoud (2015). We will focus on the trajectories implementation of the technique. The initial results for the matter power spectrum (Bartelmann et al. 2014a) hinted that the method could match current simulations. Another advantage of this method is that it has the potential to be easily adapted to multiple cosmological models, therefore allowing predictions to be made without running numerous simulations.

In this paper, we will introduce the Cosmological Trajectories Method (CTM), which expands the trajectory around the Zel'dovich approximation. We present exact results for the matter power spectrum to leading second-order in the displacement field, in the Beyond Zel'dovich approximation, and show how an expanded version of the power spectrum can be calculated numerically in Section 2. Finally, in Section 3.3 we will compare the Beyond Zel'dovich approximation to other approximations including SPT 1-loop and LPT 1-loop. We find that the Beyond Zel'dovich approximation power spectrum matches the EUCLID EMULATOR (Knabenhans et al. 2019) more accurately than the Zel'dovich approximation above $z = 1$. We also find that the Beyond Zel'dovich approximation captures the BAO peak in the two-point correlation function more accurately than SPT 1-loop, LPT 1-loop and CLPT at $z = 0$.

2 COSMOLOGICAL TRAJECTORIES METHOD (CTM)

The fundamental idea behind KFT (Bartelmann et al. 2014a,b) is that an ensemble of dark matter particles moves dictated by some initial conditions until some redshift, z_* , when a gravitational interaction term is “switched on” as in an N-body simulation. This gravitational interaction term is then expanded perturbatively. This translates to an initial particle trajectory set by a Zel'dovich propagator, thus capturing the decaying velocity, with the addition of a gravitational correction term, the size of which is controlled by an expansion parameter, ϵ . The formalism in KFT is based on field theory and therefore involves functional integrals, which is one motivation behind the work presented in Ali-Haïmoud (2015).

In Ali-Haïmoud (2015), the KFT results were re-derived in terms of particle trajectories and the Zel'dovich approximation. The trajectory is found from the solution to the particle equations of motion,

$$\begin{aligned} \mathbf{x}(\mathbf{q}, z) = & \mathbf{x}(\mathbf{q}, z_*) + \int_z^{z_*} \frac{dz'}{a'H(z')} \mathbf{u}(\mathbf{q}, z_*) \\ & - \epsilon \int_z^{z_*} \frac{dz'}{a'H(z')} \int_{z'}^{z_*} \frac{dz''}{H(z'')} \nabla \phi(\mathbf{x}(\mathbf{q}, z''), z''), \end{aligned} \quad (1)$$

where z_* is the redshift when the gravitational terms are “switched on”, z is redshift, a is the scale factor, H is the Hubble parameter, ϕ is the gravitational potential, \mathbf{x} and \mathbf{q} are the Eulerian and Lagrangian positions and $\mathbf{u} = a\mathbf{v}$ where \mathbf{v} is the proper velocity. In Ali-Haïmoud

(2015) the initial position $\mathbf{x}(\mathbf{q}, z_*)$ and velocity $\mathbf{u}(\mathbf{q}, z_*)$ at time z_* are set by the Zel'dovich approximation. The gravitational interaction term, the final term in Equation (1), is found via the Poisson equation and the overdensity field, calculated in the Zel'dovich approximation. The final result derived in Ali-Haimoud (2015) is the power spectrum to first-order in this interaction term but is exact for the Zel'dovich density field.

The result and method presented in Ali-Haimoud (2015) is very promising. However in both that approach, and in KFT, the correct linear growth is not recovered on large scales from the expansion of Equation (1). This is because to the lowest-order gravitational interaction takes too long to overcome the damping effect of the expansion, leading to an underestimate of the displacement of particles and growth of structure. In both cases a re-normalisation of the predicted linear matter-density power spectrum is required.

This problem motivates us to introduce the Cosmological Trajectories Method (CTM), which expands the gravitational interaction around the free-field Zel'dovich approximation. This guarantees that to first order in the displacement we match linear theory, and to second-order we include the effects of gravitational scattering. This expansion avoids the non-local gravitational terms that appear at second-order in LPT (Matsubara 2008a,b, Buchert & Ehlers 1993). One issue is that the free-field Zel'dovich approximation is already an approximation to gravitational collapse, so to avoid double-counting terms we remove a linear term from the gravitational interaction. A full derivation of the CTM is given in Appendix A and the CTM trajectory is presented in Equation (A2).

In this paper, we will focus on the implementation where the gravitational interaction term in the CTM trajectory is expanded to second order in the displacement field. We shall refer to this as the Beyond Zel'dovich approximation, where the trajectory is given by (see Appendix A for a full derivation)

$$x_i(\mathbf{q}, z) = q_i + A(z) \Psi_i(\mathbf{q}, z_i) + B_\epsilon(z) \Psi_j(\mathbf{q}, z_i) \left(E_{ij}(\mathbf{q}, z_i) + \frac{1}{3} \delta^{(0)}(\mathbf{q}, z_i) \delta_{ij} \right) \quad (2)$$

Here q_i is the initial Lagrangian position of the particles, Ψ_i is the linear displacement field, $\delta^{(0)}$ is the linear overdensity field,

$$E_{ij} = \left(\nabla_i \nabla_j \nabla^{-2} - \frac{1}{3} \delta_{ij} \right) \delta^{(0)}, \quad (3)$$

is a dimensionless, trace-free linear tidal tensor, and z_i is some initial redshift. Equation (2) is the leading lowest-order gravitational correction to the Zel'dovich approximation, describing post-Born gravitational deflections from the unperturbed trajectory.

As we are expanding around the Zel'dovich approximation, the linear time-dependence function in Equation (2) is $A(z) = \frac{D_1(z)}{D_1(z_i)}$. We note there is freedom to choose other time-dependencies, but this ensures the lowest-order theory matches linear growth on large scales. The second time-dependent function $B_\epsilon(z)$ in Equation (2) is derived in Appendix A to match the gravitational field, and is given by

$$B_\epsilon(z) = -\epsilon_{\text{CTM}} \omega_0^2 \int_{z_i}^z \frac{dz'}{a'H(z')} \int_{z_i}^{z'} \frac{dz''}{H(z'')} \left(\frac{D_1(z'')}{D_1(z_i)} \right)^2. \quad (4)$$

where ϵ_{CTM} controls the size of the higher-order gravitational term (the tidal tensor) and $\omega_0^2 = H_0^2 \Omega_m$. Note that in principle one could use the linear growth factor for a scale-independent modified gravity theory (Clifton et al. 2012, Nojiri et al. 2017) instead. Comparing the

Beyond Zel'dovich approximation time dependence to that obtained in Bartelmann et al. (2014a,b) and Ali-Haimoud (2015), we see that as we do not include the initial, decaying velocity term. Instead the particle follows a Zel'dovich trajectory and the displacement field is therefore proportional to the linear growth factor. In Appendix D more detail on the application of second-order CTM to KFT is given.

There are two free parameters in the second-order CTM trajectory; the initial redshift z_i and the expansion parameter ϵ_{CTM} . The expansion parameter, ϵ_{CTM} , controls the size of the gravitational terms. If one considers ϵ_{CTM} as a perturbative parameter then by definition it should be small ($\epsilon_{\text{CTM}} \ll 1$). However, this parameter can also be interpreted in a physical sense as controlling how large the non-linear structures being modelled are. We would expect that larger ϵ_{CTM} values will increase the impact the tidal field has on non-linear structure formation.

2.1 Calculating 2-point statistics using the CTM

In this section, we give details on the calculation of the matter-density power spectrum for the Beyond Zel'dovich trajectory. We find that, assuming Gaussian initial conditions, we can calculate an exact expression for the matter power spectrum in this approximation. In order to explore the numerical implementation of this result, we expand around the exact solution. Our numerical results are available using the CTM MODULE. We begin with the statistical properties of the linear fields.

2.1.1 Covariance matrix and correlation functions

The linear displacement field, Ψ_i , the tidal field, E_{ij} , and the linear overdensity field, $\delta^{(0)}$, are correlated Gaussian fields at the initial redshift, z_i . As we shall show, we can calculate the matter power spectrum in the Beyond Zel'dovich approximation using the statistics of Gaussian fields (Bardeen et al. 1986, van de Weygaert & Bertschinger 1996, Taylor & Watts 2000). As the fields are Gaussian, they are fully specified by their covariance matrix, \mathbf{C} , which contains the correlation of the fields with each other at two different Lagrangian points, \mathbf{q}_1 and \mathbf{q}_2 , at the initial redshift.

We define a vector of the fields at each position,

$$\mathbf{X} = \left(\Psi_i(\mathbf{q}_1), \Psi_i(\mathbf{q}_2), E_i(\mathbf{q}_1), E_i(\mathbf{q}_2), \delta^{(0)}(\mathbf{q}_1), \delta^{(0)}(\mathbf{q}_2) \right), \quad (5)$$

where $E_i = \text{vec}(\mathbf{E})$ is the 6-dimensional vectorisation of the distinct terms in the symmetric tidal tensor E_{ij} . The covariance matrix of the vector, $\mathbf{C} = \langle \mathbf{X}\mathbf{X}^T \rangle$, is given by

$$\mathbf{C} = \begin{pmatrix} C_{\Psi_1^1 \Psi_1^1} & C_{\Psi_1^2 \Psi_1^2} & C_{E_1^1 \Psi_1^1} & C_{E_1^2 \Psi_1^1} & C_{\delta_1^{(0)} \Psi_1^1} & C_{\delta_2^{(0)} \Psi_1^1} \\ C_{\Psi_1^1 \Psi_1^2} & C_{\Psi_1^2 \Psi_1^2} & C_{E_1^1 \Psi_1^2} & C_{E_1^2 \Psi_1^2} & C_{\delta_2^{(0)} \Psi_1^1} & C_{\delta_2^{(0)} \Psi_1^2} \\ C_{\Psi_1^1 E_1^1} & C_{\Psi_1^2 E_1^1} & C_{E_1^1 E_1^1} & C_{E_1^2 E_1^1} & C_{\delta_1^{(0)} E_1^1} & C_{\delta_2^{(0)} E_1^1} \\ C_{\Psi_1^1 E_1^2} & C_{\Psi_1^2 E_1^2} & C_{E_1^1 E_1^2} & C_{E_1^2 E_1^2} & C_{\delta_1^{(0)} E_1^2} & C_{\delta_2^{(0)} E_1^2} \\ C_{\Psi_1^1 \delta_1^{(0)}} & C_{\Psi_1^2 \delta_1^{(0)}} & C_{E_1^1 \delta_1^{(0)}} & C_{E_1^2 \delta_1^{(0)}} & C_{\delta_1^{(0)} \delta_1^{(0)}} & C_{\delta_2^{(0)} \delta_1^{(0)}} \\ C_{\Psi_1^1 \delta_2^{(0)}} & C_{\Psi_1^2 \delta_2^{(0)}} & C_{E_1^1 \delta_2^{(0)}} & C_{E_1^2 \delta_2^{(0)}} & C_{\delta_1^{(0)} \delta_2^{(0)}} & C_{\delta_2^{(0)} \delta_2^{(0)}} \end{pmatrix}, \quad (6)$$

where the numerical '1' and '2' indicate the position. The correlators of the linear density and displacement fields are given by

$$C_{\Psi_i \Psi_j} = \langle \Psi_i(\mathbf{q}_1) \Psi_j(\mathbf{q}_2) \rangle = \sigma_{ij}(q), \quad (7a)$$

$$C_{\delta_1^{(0)} \Psi_i} = \langle \delta^{(0)}(\mathbf{q}_1) \Psi_i(\mathbf{q}_2) \rangle = \Pi_i(q), \quad (7b)$$

$$C_{\delta_1^{(0)} \delta_2^{(0)}} = \langle \delta^{(0)}(\mathbf{q}_1) \delta^{(0)}(\mathbf{q}_2) \rangle = \xi_0(q), \quad (7c)$$

where $q = |\mathbf{q}_2 - \mathbf{q}_1|$ is the distance between points, while the correlations of the vectorised tidal field are

$$C_{E_i \Psi_j} = \langle E_i(\mathbf{q}_1) \Psi_j(\mathbf{q}_2) \rangle, \quad (8a)$$

$$C_{E_i E_j} = \langle E_i(\mathbf{q}_1) E_j(\mathbf{q}_2) \rangle, \quad (8b)$$

$$C_{E_i \delta_2^{(0)}} = \langle E_i(\mathbf{q}_1) \delta^{(0)}(\mathbf{q}_2) \rangle. \quad (8c)$$

These can be written in terms of the correlations of the tensor tidal field,

$$\langle E_{ij}(\mathbf{q}_1) \Psi_k(\mathbf{q}_2) \rangle = \Phi_{ijk}(q), \quad (9a)$$

$$\langle E_{ij}(\mathbf{q}_1) E_{kl}(\mathbf{q}_2) \rangle = \eta_{ijkl}(q), \quad (9b)$$

$$\langle E_{ij}(\mathbf{q}_1) \delta^{(0)}(\mathbf{q}_2) \rangle = \Sigma_{ij}(q). \quad (9c)$$

The correlation functions given in Equations (7) and Equations (9) are defined in Appendix B.

2.1.2 The full power spectrum

The matter-density power spectrum, $P(k)$, is defined by the correlator of the Fourier modes of the density field,

$$\langle \delta(\mathbf{k}_1) \delta(\mathbf{k}_2) \rangle = (2\pi)^3 P(k) \delta_D(\mathbf{k}_1 + \mathbf{k}_2), \quad (10)$$

where the expectation value is calculated by an ensemble average. The Fourier transform of the overdensity field is given by

$$(2\pi)^3 \delta_D(\mathbf{k}) + \delta(\mathbf{k}) = \int d^3q e^{i\mathbf{k}\cdot\mathbf{x}(q,z)}, \quad (11)$$

where \mathbf{x} is the trajectory defined in Equation (2). Therefore, the power spectrum for the second-order CTM trajectory is given by

$$P(k, z) = \int d^3q e^{i\mathbf{k}\cdot\mathbf{q}} \times \left[\left\langle e^{ik_i \Psi_j(\mathbf{q}_1, z_i) \left(A(z) \delta_{ij} + B_\epsilon(z) E_{ij}(\mathbf{q}_1, z_i) + \frac{1}{3} B_\epsilon(z) \delta^{(0)}(\mathbf{q}_1, z_i) \delta_{ij} \right) - ik_i \Psi_j(\mathbf{q}_2, z_i) \left(A(z) \delta_{ij} + B_\epsilon(z) E_{ij}(\mathbf{q}_2, z_i) + \frac{1}{3} B_\epsilon(z) \delta^{(0)}(\mathbf{q}_2, z_i) \delta_{ij} \right)} \right\rangle - 1 \right]. \quad (12)$$

We can simplify this by introducing a new vector,

$$\mathbf{K} = A(z) (k_i, -k_i, 0, 0, 0, 0), \quad (13)$$

with the same dimensionality as \mathbf{X} . If we define a new matrix \mathbf{M} , with the same dimensionality as \mathbf{C} ,

$$\mathbf{M} = \frac{i}{3} B_\epsilon k_i \begin{bmatrix} 0 & 0 & -3\delta_{jk} & 0 & -1 & 0 \\ 0 & 0 & 0 & 3\delta_{jk} & 0 & 1 \\ -3\delta_{jk} & 0 & 0 & 0 & 0 & 0 \\ 0 & 3\delta_{jk} & 0 & 0 & 0 & 0 \\ -1 & 0 & 0 & 0 & 0 & 0 \\ 0 & 1 & 0 & 0 & 0 & 0 \end{bmatrix}, \quad (14)$$

the ensemble average in Equation (12) can be rewritten in the multi-variate Gaussian form

$$\left\langle e^{ik_i \Psi_j(\mathbf{q}_1) \left(A \delta_{ij} + B_\epsilon E_{ij}(\mathbf{q}_1) + \frac{1}{3} B_\epsilon \delta^{(0)}(\mathbf{q}_1) \delta_{ij} \right) \times e^{-ik_i \Psi_j(\mathbf{q}_2) \left(A \delta_{ij} + B_\epsilon E_{ij}(\mathbf{q}_2) + \frac{1}{3} B_\epsilon \delta^{(0)}(\mathbf{q}_2) \delta_{ij} \right)} \right\rangle = \frac{1}{(2\pi)^{10}} \int d^{20}X |\det \mathbf{C}|^{-1/2} e^{-\frac{1}{2} \mathbf{X}^T \mathbf{C}^{-1} \mathbf{X}} e^{i\mathbf{K}\cdot\mathbf{X}} e^{-\frac{1}{2} \mathbf{X}^T \mathbf{M} \mathbf{X}}. \quad (15)$$

Equation (15) can be integrated, resulting in an exact expression for the matter power spectrum for the second-order CTM trajectory,

$$P(k, z) = \int d^3q e^{i\mathbf{k}\cdot\mathbf{q}} \left[|\det(1 + \mathbf{M}\mathbf{C})|^{-1/2} e^{-\frac{1}{2} \mathbf{K}^T \mathbf{C} [1 + \mathbf{M}\mathbf{C}]^{-1} \mathbf{K} - 1} \right]. \quad (16)$$

This expression is the main result of the paper.

2.1.3 Expansion of the power spectrum

While Equation (16) is exact, and the matrix manipulation can in principle be carried out numerically, the integration is highly oscillatory and can be numerically unstable. To explore the features of the Beyond Zel'dovich approximation we shall expand the solution in such a way as to take advantage of existing algorithms to treat the integration, and to compare to other methods.

The argument of the exponential in Equation (16) can be expanded;

$$\mathbf{K}^T \mathbf{C} [1 + \mathbf{M}\mathbf{C}]^{-1} \mathbf{K} \approx \mathbf{K}^T \mathbf{C} \mathbf{K} - \mathbf{K}^T \mathbf{C} \mathbf{M} \mathbf{C} \mathbf{K}. \quad (17)$$

The first term here is

$$\mathbf{K}^T \mathbf{C} \mathbf{K} = 2A^2(z) \left[k^2 \sigma_\psi^2(z_i) - k_i k_j \sigma_{ij}(q, z_i) \right], \quad (18)$$

where $\sigma_{ij}(0, z_i) = \sigma_\psi^2 \delta_{ij}$, while the second term vanishes. We can expand the determinant in Equation (16) as

$$\det(1 + \mathbf{M}\mathbf{C}) = \exp(\text{tr} \ln(1 + \mathbf{M}\mathbf{C})) \approx \exp\left(-\frac{1}{2} \text{tr} \mathbf{M}\mathbf{C}\mathbf{M}\mathbf{C}\right) \quad (19)$$

where $\text{tr}(\mathbf{M}\mathbf{C}) = 0$ and,

$$\text{tr}(\mathbf{M}\mathbf{C}\mathbf{M}\mathbf{C}) = \frac{4}{9} B_\epsilon^2 k_i k_j \left[\Pi_i(q) \Pi_j(q) + 6\sigma_{in}(q) \Sigma_{nj}(q) + \xi_0(q) \sigma_{ij}(q) - \xi_0(0) \sigma_\psi^2 \delta_{ij} \right]. \quad (20)$$

In this approximation the power spectrum is

$$P(k, z) = \int d^3q e^{i\mathbf{k}\cdot\mathbf{q}} \left[e^{-\frac{1}{2} [\mathbf{K}^T \mathbf{C} \mathbf{K} - \text{tr}(\mathbf{M}\mathbf{C}\mathbf{M}\mathbf{C})]} - 1 \right]. \quad (21)$$

To lowest order this reduces to the Zel'dovich power spectrum (Taylor 1993, Schneider & Bartelmann 1995, Taylor & Hamilton 1996). Both of the terms in the exponential in equation (21) have a factor $k_i k_j$, so the function is Gaussian. The covariance of this Gaussian is the differential displacement covariance. Hence, we can interpret the extra term as the lowest-order correction to the displacement covariance matrix due to gravitational scattering.

2.1.4 Numerically calculating the full expanded power spectrum

It is useful to define the correlation function $\bar{\Sigma}_{ij}(q) = \langle \bar{E}_{ij}(\mathbf{q}_1) \delta^{(0)}(\mathbf{q}_2) \rangle$, which can be related to the un-barred correlation function,

$$\bar{\Sigma}_{ij}(q) = \Sigma_{ij}(q) + \frac{1}{3} \xi_0(q) \delta_{ij}. \quad (22)$$

The correlations σ_{ij} , Π_i and $\bar{\Sigma}_{ij}$ can be split into irreducible components (Vlah et al. 2015a, Catelan et al. 2000, Crittenden et al. 2001). The method used to split σ_{ij} , Π_i and $\bar{\Sigma}_{ij}$ is shown in Appendix B1. The correlations Π_i and $\bar{\Sigma}_{ij}$ can be expanded as

$$\bar{\Sigma}_{ij}(q) = D(q) \delta_{ij} + F(q) \hat{q}_i \hat{q}_j, \quad (23)$$

$$\Pi_i(q) = G(q) \hat{q}_i. \quad (24)$$

and D , F and G are defined as

$$D(q) = \frac{1}{6\pi^2} \int_0^\infty dk [j_0(kq) + j_2(kq)] k^2 P_L(k), \quad (25a)$$

$$F(q) = -\frac{1}{2\pi^2} \int_0^\infty dk j_2(kq) k^2 P_L(k), \quad (25b)$$

$$G(q) = -\frac{1}{2\pi^2} \int_0^\infty dk j_1(kq) k P_L(k). \quad (25c)$$

Finally, the correlation of the displacement field can be decomposed as,

$$\sigma_{ij} = \left(\sigma_\psi^2 - \frac{1}{2} X'(q) \right) \delta_{ij} - \frac{1}{2} Y'(q) \hat{q}_i \hat{q}_j, \quad (26)$$

with

$$X'(q) = \frac{1}{2\pi^2} \int_0^\infty dk \left[\frac{2}{3} - 2 \frac{j_1(kq)}{kq} \right] P_L(k, z_i) \quad (27)$$

$$Y'(q) = \frac{1}{2\pi^2} \int_0^\infty dk \left[6 \frac{j_1(kq)}{kq} - 2j_0(kq) \right] P_L(k, z_i).$$

Substituting the decomposed correlations into Equation (20) then splitting the integral into k^2 and $k^2 \mu^2$ parts using the method for numerically calculating the Zel'dovich power spectrum described in Schneider & Bartelmann (1995), Carlson et al. (2013), Sugiyama (2014) and Vlah et al. (2015a). We can use the k th moment of the integral to calculate the angular integral

$$I_k = \int_{-1}^1 d\mu \mu^k e^{ia\mu} e^{b^2 \mu^2} \quad (28)$$

which can be solved using the general prescription (Schneider & Bartelmann 1995, Vlah et al. 2015a),

$$I_k = 2 (-i)^k e^b \sum_{n=0}^{\infty} (-2b)^n \left(\frac{d}{dk} \right)^k a^{-n} j_n(a), \quad (29)$$

where j_n is a spherical Bessel function. The angular parts of Equation (16) are calculated using an identity resulting in the power spectrum becoming,

$$P(k, z) \approx 2\pi \int_0^\infty dq q^2 \int_{-1}^1 d\mu e^{ikq\mu} \left[e^{-\frac{1}{2} k^2 A^2 (X' + \mu^2 Y')} e^{B_\epsilon^2 k^2 (W' + \mu^2 Z')} - e^{-k^2 \sigma_\psi^2 (A^2 + \frac{1}{3} B_\epsilon^2 \eta_E^2)} \right], \quad (30)$$

where the second exponential term is a Dirac delta function at the origin and has been added to cancel oscillations as described in Schneider & Bartelmann (1995). The Beyond Zel'dovich power spectrum to second-order is finally given by

$$P(k, z) = 4\pi \int_0^\infty dq q^2 e^{-\frac{1}{2} k^2 [A^2 (X' + Y') - 2B_\epsilon^2 (W' + Z')]} \times \sum_{n=0}^{\infty} \left[\frac{k (A^2 Y' - 2B_\epsilon^2 Z')}{q} \right]^n j_n(kq) \quad (31)$$

where

$$W' = -\frac{1}{3} \sigma_\psi^2 \eta_E^2 + \frac{1}{3} \left(\sigma_\psi^2 - \frac{1}{2} X' \right) \left(2D - \frac{1}{3} \xi_0^2 \right), \quad (32a)$$

$$Z' = \frac{1}{9} G^2 + \frac{2}{3} \left(\sigma_\psi^2 - \frac{1}{2} X' \right) F - \frac{1}{3} Y' \left(D + F - \frac{1}{6} \xi_0^2 \right). \quad (32b)$$

In the above expressions for W' and Z' all functions apart from σ_ψ^2 and η_E^2 are evaluated at q .

3 THE BEYOND ZEL'DOVICH APPROXIMATION

The power spectra presented in the remainder of this paper have been calculated using the CTM MODULE¹. The initial power spectra and cosmological parameters are calculated using CLASSYLS² and the spherical Bessel integrals are calculated using MCFIT³. The power spectra are calculated using Planck18 (Planck Collaboration et al. 2020) cosmology ($\Omega_m = 0.3123$, $h = 0.6737$, $n_s = 0.9665$ and $\sigma_8 = 0.8102$). We also sum over $n = 32$ spherical-Bessel functions when calculating the power spectra. See Appendix C for more details on the numerical integration tools used in the CTM MODULE.

There are two free parameters in the second-order CTM trajectory: the initial redshift, z_i , and the expansion parameter, ϵ_{CTM} . The choice of the initial redshift does not make a noticeable difference to the final power spectrum unless a very low value such as $z_i = 10$ is chosen. Since we assume that the fields are initially Gaussian a sufficiently high value of z_i must be chosen to not invalidate the method. In this paper, we will set $z_i = 100$.

Recall that, the Beyond Zel'dovich approximation is the second-order CTM trajectory where the linear displacement terms are proportional to the linear growth factor. In Figure 1, the dimensionless Beyond Zel'dovich power spectrum calculated with three ϵ_{CTM} values, $\epsilon_{\text{CTM}} = 0.01, 0.1, 1$ at $z = 0$ is shown in the top-left panel, at $z = 1$ in the top-right panel, at $z = 2$ in the lower-left panel and at $z = 3$ in the lower-right panel. Results from the EUCLID EMULATOR⁴ (Knabenhans et al. 2019) are shown in dashed grey lines. In Knabenhans et al. (2019), the emulator is found to be $\pm 1\%$ accurate compared to simulations at $z = 0$ and $\pm 1\%$ up to $k = 1 \text{ h Mpc}^{-1}$ at $z = 1$. Above $z = 1$ it is around $\approx 3\%$ accurate. The emulator was built on a sample of 100 input runs of PKDGRAV3 (Stadel et al. 2002, Potter et al. 2017).

The power spectra shown in Figure 1 have been truncated at $k = 0.9 \text{ h Mpc}^{-1}$. The second-order CTM trajectory is only applicable until this k -value as the method suffers from numerical issues

¹ <https://github.com/franlane94/CTM>

² <https://classyls.readthedocs.io/en/stable/>

³ <https://github.com/eelregit/mcfit>

⁴ [https://github.com/miknab/EuclidEmulator/wiki/III\)-Usage](https://github.com/miknab/EuclidEmulator/wiki/III)-Usage)

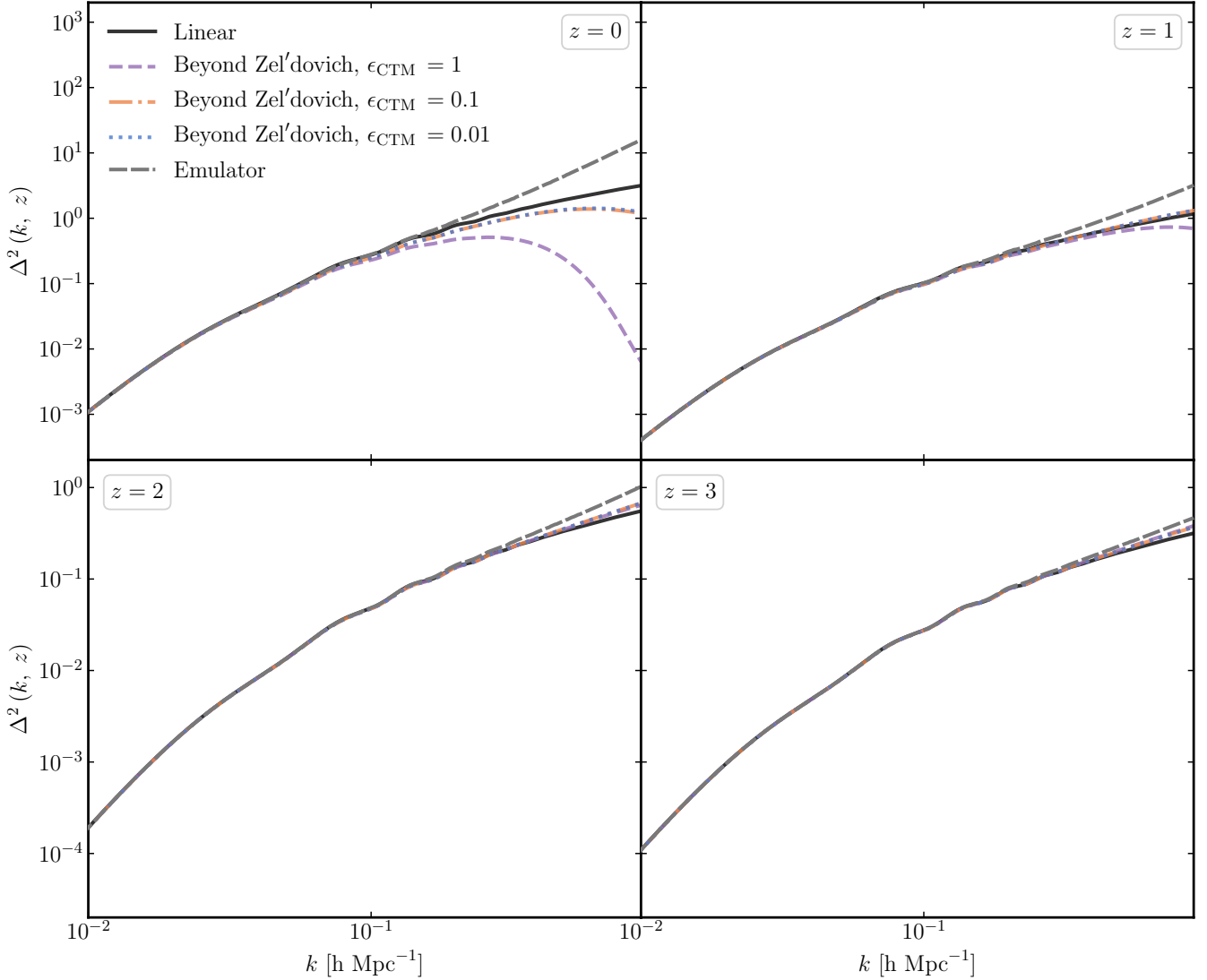


Figure 1. The dimensionless power spectrum for linear theory (black solid line), Beyond Zel'dovich with $\epsilon_{\text{CTM}} = 1$ (dashed purple line), Beyond Zel'dovich with $\epsilon_{\text{CTM}} = 0.1$ (dashed-dot orange line) and Beyond Zel'dovich with $\epsilon_{\text{CTM}} = 0.01$ (dotted blue line) at $z = 0$ in the top-left panel, at $z = 1$ top-right panel, at $z = 2$ in the lower-left panel and at $z = 3$ in the lower-right panel. The EUCLID EMULATOR result is shown in by grey dashed line in at the relevant redshift all panels.

beyond this point and it is difficult to disentangle these from physical effects. This is addressed in Appendix C. At all redshifts, the Beyond Zel'dovich approximation calculated with $\epsilon_{\text{CTM}} = 0.1$ and $\epsilon_{\text{CTM}} = 0.01$ appears to have little effect on the trajectory. This was to be expected as the ϵ_{CTM} parameter controls the size of the gravitational correction to the Zel'dovich trajectory. The Beyond Zel'dovich approximation with $\epsilon_{\text{CTM}} = 1$ performs well at redshifts above $z = 2$ compared to the EUCLID EMULATOR. However, at low redshifts the power spectrum is not boosted on small-scales, rather it is excessively damped. This is most likely due to shell-crossing and the particle trajectories overshooting on small-scales. We will present a solution to this excessive damping in Section 3.1.

The effect of the ϵ_{CTM} parameter on the Beyond Zel'dovich power spectrum is shown in more detail in Figure 2. The maximum k -value reached before the difference,

$$\Delta_{\text{diff}} = \frac{P_{\text{calc}}(k) - P_{\text{emu}}(k)}{P_{\text{emu}}(k)}, \quad (33)$$

where P_{emu} is the power spectrum obtained using the EUCLID EMULATOR exceeds $\Delta_{\text{diff}} = \pm 0.05$ is shown.

One can see more clearly that the Beyond Zel'dovich approximation calculated with smaller values of ϵ_{CTM} (shown in blue plus signs and orange crosses) converges to the Zel'dovich approximation (shown in black circles). This validates our approximation as if $\epsilon_{\text{CTM}} = 0$ the Beyond Zel'dovich approximation reduces to the Zel'dovich approximation. To have any improvement over the Zel'dovich approximation at high redshifts, we must have a value of $\epsilon_{\text{CTM}} = 1$ (shown in purple diamonds). The Beyond Zel'dovich results in the remainder of this paper will be calculated with this value.

3.1 A Gaussian damped initial power spectrum

To reduce the impact of the small-scale breakdown on larger scales, we will introduce a Gaussian damped initial power spectrum defined

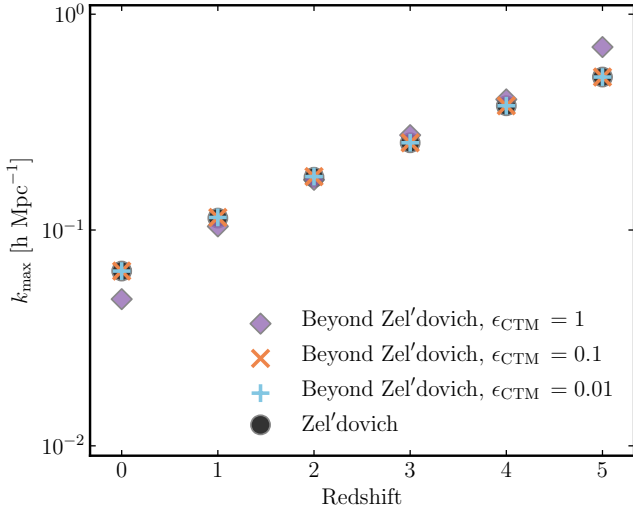


Figure 2. The maximum k -value reached, k_{\max} , before the difference between the Beyond Zel'dovich approximation and the EUCLID EMULATOR exceeds $\pm 5\%$ versus redshift. The purple diamonds represent the Beyond Zel'dovich approximation calculated with $\epsilon_{\text{CTM}} = 1$, the orange crosses are calculated with $\epsilon_{\text{CTM}} = 0.1$ and the blue plus signs with $\epsilon_{\text{CTM}} = 0.01$. The black circles represent the Zel'dovich approximation.

as

$$P_{\text{damped}}(k, z) = e^{-\left(\frac{k}{k_c}\right)^2} P_{\text{L}}(k, z) \quad (34)$$

where k_c is the cut-off scale.

In Figure 3, the maximum k -value reached before the difference between the calculated Beyond Zel'dovich power spectrum and the emulator power spectrum becomes larger than $\Delta_{\text{diff}} = \pm 5\%$ is shown versus redshift. The Beyond Zel'dovich power spectra were calculated using $\epsilon_{\text{CTM}} = 1$ and an initial Gaussian damped power spectrum with $k_c = 50 \text{ h Mpc}^{-1}$ (blue plus signs), $k_c = 5 \text{ h Mpc}^{-1}$ (purple diamonds) and $k_c = 0.5 \text{ h Mpc}^{-1}$ (orange crosses). The highest cut-off value of $k_c = 50 \text{ h Mpc}^{-1}$ has no noticeable effect and the lowest cut-off value of $k_c = 0.5 \text{ h Mpc}^{-1}$ does not counteract the over damping on small scales until $z = 0$. The largest and smallest cut-off values are too stringent and either restrict structure formation too much or too little in the desired regime. The value of $k_c = 5 \text{ h Mpc}^{-1}$, however, appears to effectively remove the influence of the breakdown on larger scales at a wide range of redshifts.

Therefore, in Figure 4 a range of cut-off values centered around $k_c = 5 \text{ h Mpc}^{-1}$ are tested. As was the case previously small cut-off values ($k_c < 4 \text{ h Mpc}^{-1}$) have a detrimental effect on structure formation at high redshifts. We will choose to set $k_c = 6 \text{ h Mpc}^{-1}$ to remove the effect of the breakdown on the Beyond Zel'dovich power spectrum for as wide a redshift range as possible. Hence, in all future plots the Beyond Zel'dovich power spectra are calculated with an initial Gaussian damped power spectrum with $k_c = 6 \text{ h Mpc}^{-1}$.

Although not shown in this paper, we tested the dependence of the cut-off parameter k_c on the cosmology chosen. We compared the value of k_{\max} reached when the damped power spectrum was calculated using a value of $\Omega_m = 0.3123$ and a value of $\Omega_m = 0.3155$ (note all other cosmological parameters were kept the same). We found that there was a small difference of $\sim 5\%$ on average, implying that the cut-off scale is likely only weakly dependent on both cosmology and redshift. As we were comparing our results to the EUCLID EMULATOR we were limited in the range of Ω_m values we

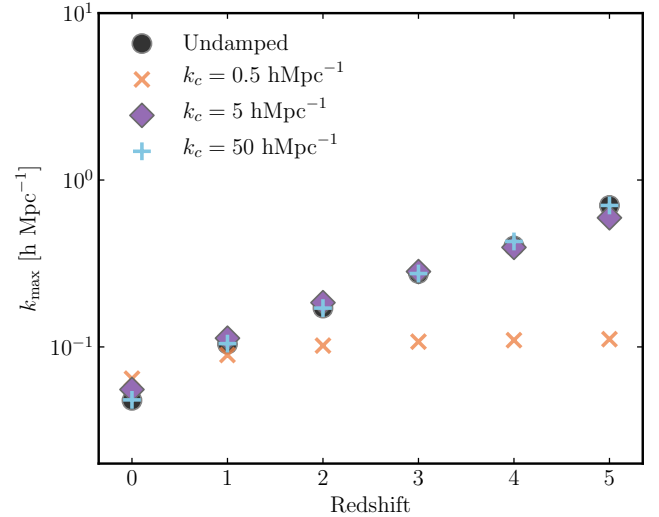


Figure 3. The maximum k -value reached before the difference between the Beyond Zel'dovich approximation power spectrum, calculated with $\epsilon_{\text{CTM}} = 1$ and an initial Gaussian damped power spectrum shown in Equation (34), becomes larger than $\pm 5\%$ is shown vs. redshift.

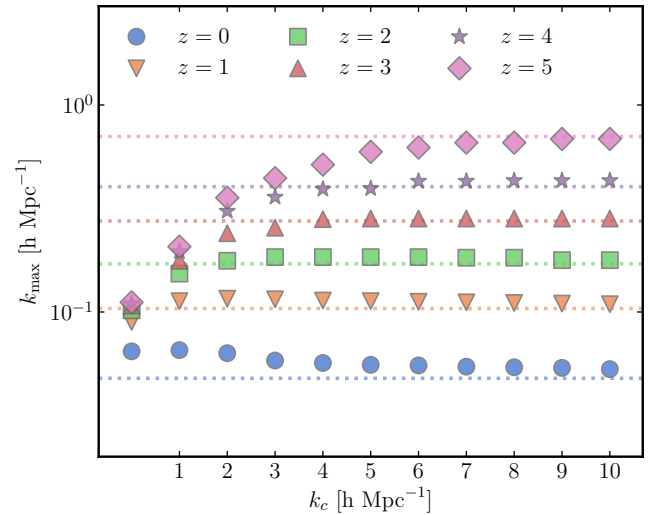


Figure 4. The maximum k -value reached before the difference between the Beyond Zel'dovich approximation power spectrum, calculated with $\epsilon_{\text{CTM}} = 1$ and an initial Gaussian damped power spectrum in Equation (34), becomes larger than $\pm 5\%$ is shown vs. the cut-off value k_c .

could choose. We leave it to future work to obtain simulation data for a wider range of cosmological parameters to more stringently test the dependence of the cut-off on cosmology.

3.2 Comparing the Beyond Zel'dovich approximation correlation function to other methods

In this section, we will investigate the performance of the Beyond Zel'dovich approximation for modelling the two-point correlation function. Specifically, we are interested in modelling the mildly non-linear regime, as this is where we find the BAO signal

($r \approx 100 \text{ Mpc h}^{-1}$ or $k \approx 0.01 \text{ h Mpc}^{-1}$) first detected in Eisenstein et al. (2005) and Cole et al. (2005). In Figure 5, the solid lines show the scaled correlation functions for the Beyond Zel’dovich approximation (upper-left panel), SPT 1-loop (upper-right panel) as discussed in Crocce & Scoccimarro (2006a,b), Taruya & Hiramoto (2008), Bernardeau et al. (2008, 2012, 2014), Blas et al. (2014), LPT 1-loop (lower-left panel) as described in Matsubara (2008a,b), Carlson et al. (2009), Vlah et al. (2015a), Sugiyama (2014), Carlson et al. (2013), McQuinn & White (2016), Vlah et al. (2015a) and CLPT (lower-right panels) as described in Carlson et al. (2013), Wang et al. (2013), Vlah et al. (2015a,b, 2016b). The different colours represent redshifts $z = 0$ to $z = 3$ and the squares show the results from the EUCLID EMULATOR. In all comparison figures, the solid lines represent the Beyond Zel’dovich approximation.

One can see that above $z = 1$ all perturbative schemes and approximations match the emulator results well. This is to be expected as the non-linear effects that cause the spatial deformation of the BAO peak are small. In SPT 1-loop, the BAO peak is expected to grow in amplitude over time. This is true, however, the peak is expected to remain the same spatially. This is not accurate as bulk flows disrupt the shape of the peak (McQuinn & White 2016). This is why in the upper right panel SPT 1-loop does not capture the BAO peak.

The Beyond Zel’dovich approximation (upper-left panel), LPT 1-loop (lower-left panel), CLPT (lower-right panel), on the other hand, capture both the BAO peak and the small scales well. Both CLPT and the Beyond Zel’dovich approximation appear to be marginally less accurate on small scales than LPT 1-loop. Again, the performance of these methods is as expected. Methods based on the Zel’dovich approximation model the spatial evolution of the BAO peak more accurately due to their more precise modelling of spatial deformation.

In Figure 6, the difference between the Beyond Zel’dovich, Zel’dovich approximation, LPT 1-loop and CLPT correlation functions and the emulator results are shown at $z = 0$. The Beyond Zel’dovich approximation matches the EUCLID EMULATOR more closely in the mildly non-linear regime than CLPT. The accuracy of the Beyond Zel’dovich approximation in the BAO peak regime is due to the inclusion of the tidal field term in Equation (2), as the spatial deformation responsible for the non-linear evolution of the BAO peak, is encoded within the tidal tensor.

3.3 Comparing the Beyond Zel’dovich approximation power spectrum to other methods

In this section, we will compare the Beyond Zel’dovich approximation (with $\epsilon_{\text{CTM}} = 1$ and $k_c = 6 \text{ h Mpc}^{-1}$) power spectrum calculated using the CTM MODULE to other methods. The first method we compared the Beyond Zel’dovich approximation to is the Zel’dovich approximation which has also been computed with an initial Gaussian damped power spectrum. In Figure 7, the top-left panel shows the difference between the Beyond Zel’dovich (solid lines) and Zel’dovich (dashed) power spectra at different redshifts. Above $z = 1$ the Beyond Zel’dovich approximation matches the EUCLID EMULATOR results more consistently.

In the upper-right hand panel of Figure 7, the difference between the Beyond Zel’dovich approximation and SPT 1-loop (dashed lines) is shown for a range of redshifts. The SPT 1-loop power spectra and correlation function were calculated using FASTPT (McEwen et al. 2016, Fang et al. 2017). SPT 1-loop models the non-linear regime more accurately than the Beyond Zel’dovich approximation at all redshifts. However, in Section 3.2 we observed that SPT 1-loop does not model the BAO feature in the correlation function as accurately as other methods.

The difference between the Beyond Zel’dovich approximation power spectrum, that obtained for LPT 1-loop and the emulator is shown in the lower left panel of Figure 7. At redshifts less than $z = 4$, LPT 1-loop models structure formation on small scales more accurately. For redshifts $z = 4$ and $z = 5$, the Beyond Zel’dovich approximation performs as well as LPT 1-loop until around $k = 0.1 \text{ h Mpc}^{-1}$.

Finally, in the bottom-right panel the Beyond Zel’dovich approximation is compared to 3-point Convolution Lagrangian Perturbation Theory (CLPT) and computed using CLEFT⁵ (the CLPT correlation function presented in Section 3.2 was also calculated this way). Again CLPT matches the emulator results more stringently in the non-linear regime at all redshifts compared to the Beyond Zel’dovich approximation. In summary, the Beyond Zel’dovich approximation is more accurate than the Zel’dovich approximation above redshift $z = 1$ and matches LPT 1-loop until around $k = 0.1 \text{ h Mpc}^{-1}$.

4 CONCLUSIONS

In this paper, we have introduced the Cosmological Trajectories Method (CTM). The leading second-order CTM trajectory, the Beyond Zel’dovich approximation is comprised of the Zel’dovich approximation with a gravitational correction term given by the product of the linear displacement field and a tidal tensor. This post-Born approximation to the Zel’dovich approximation should capture non-linear effects such as gravitational deflection. We then introduced a special case of second-order CTM called the Beyond Zel’dovich approximation in which the linear order terms were proportional to the linear growth factor, D_1 . We have calculated the exact expression for the Beyond Zel’dovich matter power spectrum, assuming Gaussian initial conditions. A numerical implementation of this expands around this solution, for stability. The Beyond Zel’dovich approximation computed with an initial Gaussian damped power spectrum outperformed the Zel’dovich approximation (also computed with an initial Gaussian damped power spectrum) when compared to the power spectrum obtained using the EUCLID EMULATOR at redshifts above $z = 1$. The Beyond Zel’dovich approximation also matched the emulator correlation function between $r = 5 \text{ Mpc h}^{-1}$ and $r = 10 \text{ Mpc h}^{-1}$ as well as SPT 1-loop, LPT 1-loop and CLPT at $z = 0$. As demonstrated in Figure 6 the Beyond Zel’dovich approximation further models the BAO peak in the correlation function more accurately than the Zel’dovich approximation, SPT 1-loop and CLPT at $z = 0$.

The Beyond Zel’dovich approximation power spectrum also matched the performance of LPT 1-loop until $k = 0.1 \text{ h Mpc}^{-1}$ when compared to the emulator power spectrum above $z = 1$. Although LPT 1-loop, SPT 1-loop and CLPT outperformed the Beyond Zel’dovich approximation on small scales ($k \geq 0.5 \text{ h Mpc}^{-1}$), on mildly non-linear scales the Beyond Zel’dovich approximation matched the emulator power spectrum. This suggests that the CTM could be implemented to produce mock observables for future BAO observations taken by instruments such as DESI in its current state.

We investigated and fixed the two free parameters of the theory, ϵ_{CTM} which controls the size of the correction term, and z_i the initial redshift at which the correlations of the fields are calculated at to be $\epsilon_{\text{CTM}} = 1$ and $z_i = 100$. On small scales ($k \geq 1 \text{ h Mpc}^{-1}$) numerical integration issues were encountered, resulting in the distrust of results beyond this point. The numerical issues and possible solutions were discussed in Appendix C. We introduced an initial Gaussian damped

⁵ <https://github.com/modichirag/CLEFT>

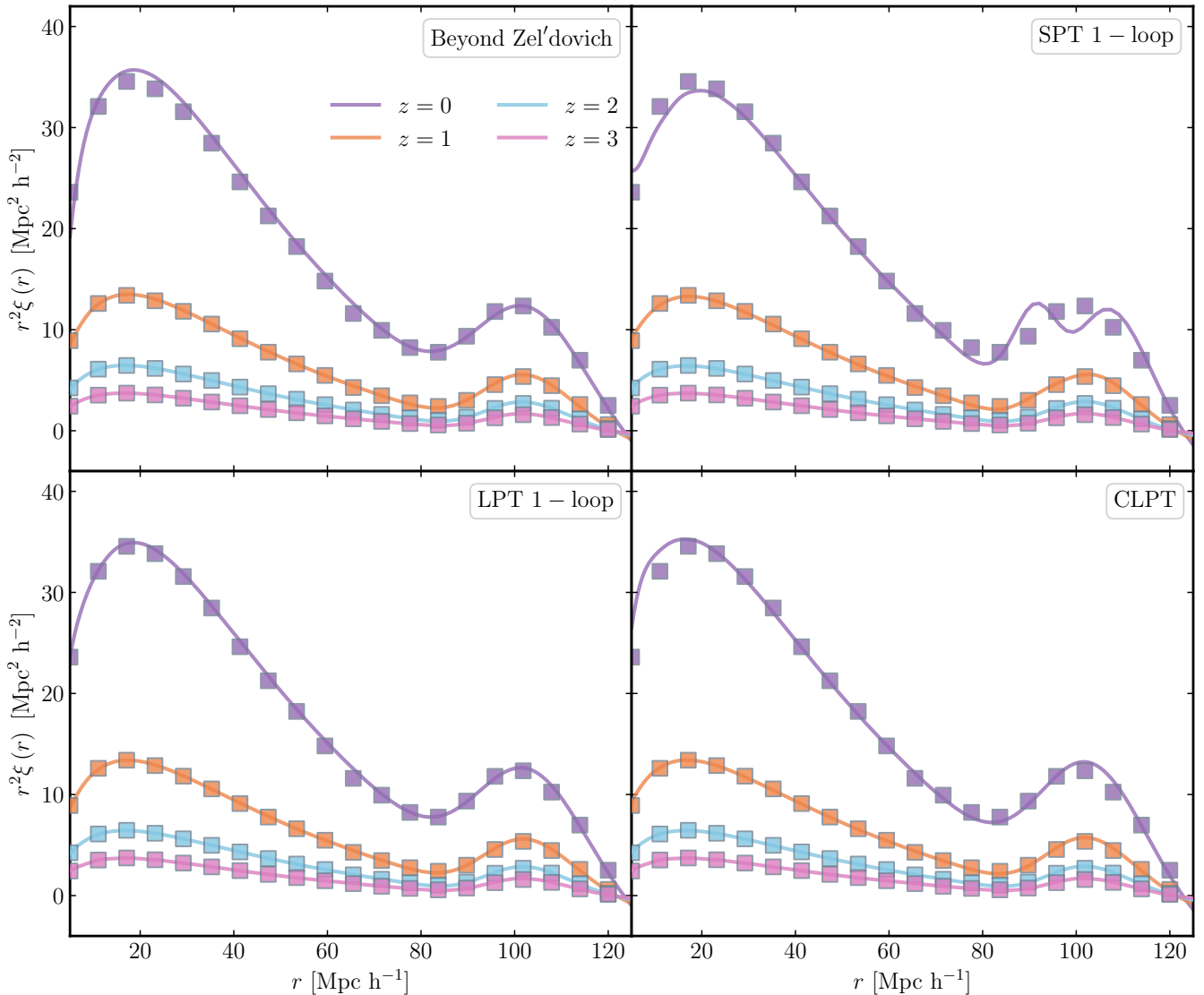


Figure 5. The scaled two-point correlation function calculated using the Beyond Zel’dovich approximation (upper-left panel), SPT 1-loop (upper-right panel), LPT 1-loop (lower-left panel) and CLPT (lower-right panel) is shown for four redshifts ($z = 0$ in purple, $z = 1$ in orange, $z = 2$ in blue, $z = 3$ in pink). The results from the EUCLID EMULATOR are shown in squares.

power spectrum with a cut-off scale of $k_c = 6 \text{ h Mpc}^{-1}$ to reduce the excessive damping on mildly non-linear scales due to shell-crossing showed in Figure 1. We leave it to future work to investigate the dependence of this Gaussian cut-off on both cosmology and redshift as it may have an impact on the application of the CTM to modified gravity theories or large deviations from Λ -CDM cosmology.

In conclusion, both the CTM and the Beyond Zel’dovich approximation appear to be valuable tools for studying nonlinear clustering of matter and galaxies in the Universe. The Beyond Zel’dovich approximation can be used to interpret future BAO observations by instruments such as *DESI* and *LSST*. Furthermore, both approximations could be used in conjunction with Lyman- α observations, re-ionisation studies and other high redshift surveys, as we verified that our approach performs particularly well at higher redshift. Thus, the CTM promises to enable placing even tighter statistical constraints on viable models of dark matter and dark energy, as well as on modified gravity theories.

ACKNOWLEDGEMENTS

The authors would like to thank Matthias Bartelmann, Yacine Ali-Haimoud, Zvonimir Vlah and Yanchuan Cai for useful discussions. F.C. Lane acknowledges the support of the UK Science and Technology Facilities Council and the Scottish Universities Physics Alliance. A.N. Taylor thanks the Royal Society for the support of a Wolfson Research Merit Award and a STFC Consolidated Grant. D. Sorini is supported by the European Research Council, under grant no. 670193.

REFERENCES

- Abbott T. M. C., et al., 2018, *MNRAS*, **480**, 3879
 Ali-Haimoud Y., 2015, *Phys. Rev. D*, **91**, 103507
 Bardeen J. M., Bond J. R., Kaiser N., Szalay A. S., 1986, *ApJ*, **304**, 15

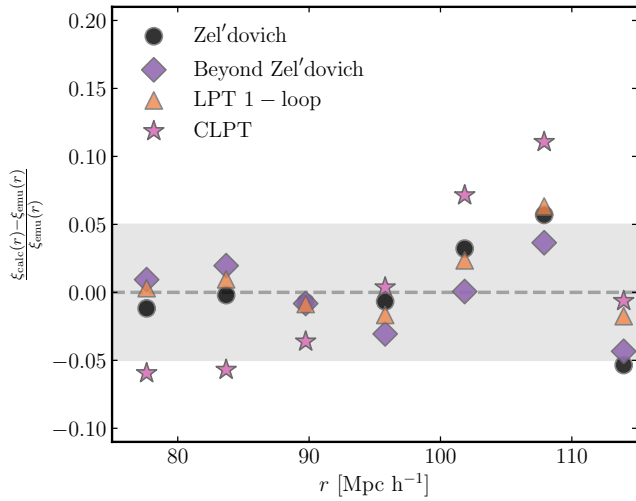


Figure 6. The difference, Δ_{diff} , between the Beyond Zel'dovich (purple diamonds), Zel'dovich approximation (black circles), LPT 1-loop (orange triangles) and CLPT (blue stars) correlation functions and the EUCLID EMULATOR at $z = 0$. The grey shaded region shows $\Delta_{\text{diff}} \pm 0.05$.

Bartelmann M., Fabis F., Berg D., Kozlikin E., Lilow R., Viermann C., 2014a, arXiv e-prints, p. [arXiv:1411.1153](#)

Bartelmann M., Fabis F., Berg D., Kozlikin E., Lilow R., Viermann C., 2014b, arXiv e-prints, p. [arXiv:1411.1502](#)

Bartelmann M., Fabis F., Kozlikin E., Lilow R., Dombrowski J., Mildenerger J., 2017, *New Journal of Physics*, **19**, 083001

Bartelmann M., et al., 2019, *Annalen der Physik*, **531**, 1800446

Bernardeau F., 2013, arXiv e-prints, p. [arXiv:1311.2724](#)

Bernardeau F., Colombi S., Gaztañaga E., Scoccimarro R., 2002, *Phys. Rep.*, **367**, 1

Bernardeau F., Crocce M., Scoccimarro R., 2008, *Phys. Rev. D*, **78**, 103521

Bernardeau F., Crocce M., Scoccimarro R., 2012, *Phys. Rev. D*, **85**, 123519

Bernardeau F., Taruya A., Nishimichi T., 2014, *Phys. Rev. D*, **89**, 023502

Bertschinger E., 1995, Technical report, Cosmological dynamics

Blas D., Garny M., Konstandin T., 2014, *Journal of Cosmology and Astro-Particle Physics*, **2014**, 010

Bouchet F. R., 1996, in Bonometto S., Primack J. R., Provenzale A., eds, *Dark Matter in the Universe*. p. 565 ([arXiv:astro-ph/9603013](#))

Bouchet F. R., Colombi S., Hivon E., Juszkiewicz R., 1995, *A&A*, **296**, 575

Buchert T., 1992, *MNRAS*, **254**, 729

Buchert T., Ehlers J., 1993, *MNRAS*, **264**, 375

Carlson J., White M., Padmanabhan N., 2009, *Phys. Rev. D*, **80**, 043531

Carlson J., Reid B., White M., 2013, *MNRAS*, **429**, 1674

Carrasco J. J. M., Hertzberg M. P., Senatore L., 2012, *Journal of High Energy Physics*, **2012**, 82

Carrasco J. J. M., Foreman S., Green D., Senatore L., 2014a, *Journal of Cosmology and Astro-Particle Physics*, **2014**, 056

Carrasco J. J. M., Foreman S., Green D., Senatore L., 2014b, *Journal of Cosmology and Astro-Particle Physics*, **2014**, 057

Carroll S. M., Leichenauer S., Pollack J., 2014, *Phys. Rev. D*, **90**, 023518

Catelan P., 1995, *MNRAS*, **276**, 115

Catelan P., Porciani C., Kamionkowski M., 2000, *MNRAS*, **318**, L39

Clifton T., Ferreira P. G., Padilla A., Skordis C., 2012, *Physics Reports*, **513**, 1–189

Cole S., et al., 2005, *Monthly Notices of the Royal Astronomical Society*, **362**, 505–534

Crain R. A., et al., 2015, *MNRAS*, **450**, 1937

Crittenden R. G., Natarajan P., Pen U.-L., Theuns T., 2001, *ApJ*, **559**, 552

Crocce M., Scoccimarro R., 2006a, *Phys. Rev. D*, **73**, 063519

Crocce M., Scoccimarro R., 2006b, *Phys. Rev. D*, **73**, 063520

Davé R., Anglés-Alcázar D., Narayanan D., Li Q., Rafieferantsoa M. H.,

Appleby S., 2019, *Monthly Notices of the Royal Astronomical Society*, **486**, 2827–2849

DeRose J., et al., 2019, *ApJ*, **875**, 69

Dubois Y., et al., 2020, arXiv e-prints, p. [arXiv:2009.10578](#)

Eisenstein D. J., et al., 2005, *The Astrophysical Journal*, **633**, 560–574

Fabis F., Berg D., Kozlikin E., Bartelmann M., 2014, arXiv e-prints, p. [arXiv:1412.2572](#)

Fang X., Blazek J. A., McEwen J. E., Hirata C. M., 2017, *Journal of Cosmology and Astroparticle Physics*, **2017**, 030–030

Friedrich P., Prokopec T., 2017, *Phys. Rev. D*, **96**, 083504

Friedrich P., Prokopec T., 2018, *Phys. Rev. D*, **98**, 025010

Friedrich P., Prokopec T., 2019, *Phys. Rev. D*, **100**, 103527

Halle A., Nishimichi T., Taruya A., Colombi S., Bernardeau F., 2020, arXiv e-prints, p. [arXiv:2001.10417](#)

Hamilton A. J. S., 2015, FFTLog: Fast Fourier or Hankel transform ([ascl:1512.017](#))

Heitmann K., Higdon D., White M., Habib S., Williams B. J., Lawrence E., Wagner C., 2009, *The Astrophysical Journal*, **705**, 156–174

Heitmann K., White M., Wagner C., Habib S., Higdon D., 2010, *The Astrophysical Journal*, **715**, 104–121

Heitmann K., Lawrence E., Kwan J., Habib S., Higdon D., 2013, *The Astrophysical Journal*, **780**, 111

Hildebrandt H., et al., 2017, *MNRAS*, **465**, 1454

Hu W., Sawicki I., 2007, *Physical Review D*, **76**

Kim J., Park C., Rossi G., Lee S. M., Gott J. Richard I., 2011, *Journal of Korean Astronomical Society*, **44**, 217

Knabenhans M., et al., 2019, *MNRAS*, **484**, 5509–5529

Kozlikin E., Fabis F., Lilow R., Viermann C., Bartelmann M., 2014, arXiv e-prints, p. [arXiv:1412.2715](#)

LSST Science Collaboration et al., 2009, LSST Science Book, Version 2.0 ([arXiv:0912.0201](#))

Lawrence E., Heitmann K., White M., Higdon D., Wagner C., Habib S., Williams B., 2010, *The Astrophysical Journal*, **713**, 1322–1331

Lawrence E., et al., 2017, *The Astrophysical Journal*, **847**, 50

Levi M. E., et al., 2019, The Dark Energy Spectroscopic Instrument (DESI) ([arXiv:1907.10688](#))

Lilow R., Fabis F., Kozlikin E., Viermann C., Bartelmann M., 2019, *Journal of Cosmology and Astro-Particle Physics*, **2019**, 001

Matsubara T., 2008a, *Phys. Rev. D*, **77**, 063530

Matsubara T., 2008b, *Phys. Rev. D*, **78**, 083519

McDonald P., Vlah Z., 2018, *Phys. Rev. D*, **97**, 023508

McEwen J. E., Fang X., Hirata C. M., Blazek J. A., 2016, *Journal of Cosmology and Astroparticle Physics*, **2016**, 015–015

McQuinn M., White M., 2016, *Journal of Cosmology and Astro-Particle Physics*, **2016**, 043

Mehrem R., 2011, The Plane Wave Expansion, Infinite Integrals and Identities involving Spherical Bessel Functions ([arXiv:0909.0494](#))

Moutarde F., Alimi J. M., Bouchet F. R., Pellat R., Ramani A., 1991, *ApJ*, **382**, 377

Nishimichi T., et al., 2019, *ApJ*, **884**, 29

Nojiri S., Odintsov S., Oikonomou V., 2017, *Physics Reports*, **692**, 1–104

Peebles P. J. E., 1980, The large-scale structure of the universe

Pillepich A., et al., 2018, *MNRAS*, **473**, 4077

Planck Collaboration et al., 2020, *A&A*, **641**, A6

Porto R. A., Senatore L., Zaldarriaga M., 2014, *Journal of Cosmology and Astro-Particle Physics*, **2014**, 022

Potter D., Stadel J., Teyssier R., 2017, *Computational Astrophysics and Cosmology*, **4**, 2

Racca G. D., et al., 2016, *Space Telescopes and Instrumentation 2016: Optical, Infrared, and Millimeter Wave*

Ramachandra N., Valogiannis G., Ishak M., Heitmann K., 2020, Matter Power Spectrum Emulator for $f(R)$ Modified Gravity Cosmologies ([arXiv:2010.00596](#))

Rampf C., Buchert T., 2012, *Journal of Cosmology and Astroparticle Physics*, **2012**, 021–021

Schaye J., et al., 2015, *MNRAS*, **446**, 521

Schneider P., Bartelmann M., 1995, *MNRAS*, **273**, 475

Seljak U., Vlah Z., 2015, *Phys. Rev. D*, **91**, 123516

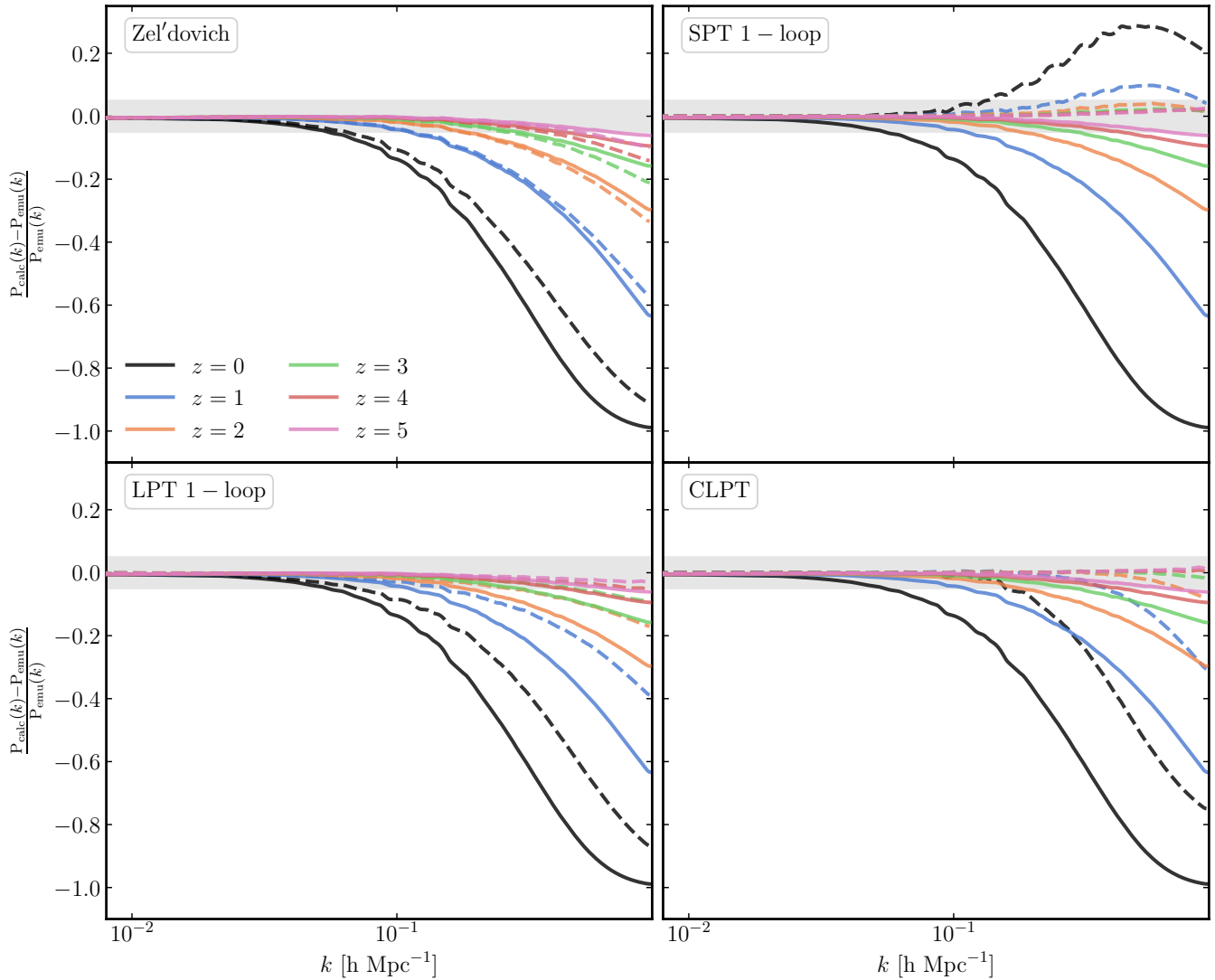


Figure 7. The difference between a given theory and the emulator results is shown for redshifts $z = 0, 1, 2, 3, 4$ and 5 . The difference between the Beyond Zel'dovich approximation and the emulator is shown in solid lines in all four panels. The differences between the Zel'dovich approximation (upper-left panel), SPT 1-loop (upper-right panel), LPT 1-loop (lower-left panel) and 3-point CLPT (lower-right panel) are shown in dashed lines. The grey shaded region shows $\Delta_{\text{diff}} \pm 0.05$.

Senatore L., Zaldarriaga M., 2015, *Journal of Cosmology and Astro-Particle Physics*, 2015, 013

Somerville R. S., Davé R., 2015, *ARA&A*, 53, 51

Sorini D., 2017, PhD thesis, International Max Planck Research School for Astronomy and Cosmic Physics at the University of Heidelberg (IMPRS-HD), Germany

Springel V., et al., 2005, *Nature*, 435, 629–636

Stadel J., Wadsley J., Richardson D. C., 2002, *High Performance Computational Astrophysics with PKDGRAV/Gasoline*. Springer US, Boston, MA, pp 501–523, doi:10.1007/978-1-4615-0849-6_32

Sugiyama N. S., 2014, *ApJ*, 788, 63

Taruya A., Colombi S., 2017, *MNRAS*, 470, 4858

Taruya A., Hiramatsu T., 2008, *ApJ*, 674, 617

Tatekawa T., 2004, *Lagrangian perturbation theory in Newtonian cosmology* (arXiv:astro-ph/0412025)

Taylor A. N., 1993, in Bouchet F., Lachieze-Rey M., eds, *Cosmic Velocity Fields*. p. 585

Taylor A. N., Hamilton A. J. S., 1996, *MNRAS*, 282, 767

Taylor A. N., Watts P. I. R., 2000, *MNRAS*, 314, 92

Uhlemann C., Rampf C., Gosenca M., Hahn O., 2019, *Phys. Rev. D*, 99, 083524

Viermann C., Fabis F., Kozlikin E., Lilow R., Bartelmann M., 2015, *Phys. Rev. E*, 91, 062120

Vlah Z., Seljak U., Baldauf T., 2015a, *Phys. Rev. D*, 91, 023508

Vlah Z., White M., Aviles A., 2015b, *Journal of Cosmology and Astro-Particle Physics*, 2015, 014

Vlah Z., Seljak U., Yat Chu M., Feng Y., 2016a, *Journal of Cosmology and Astro-Particle Physics*, 2016, 057

Vlah Z., Castorina E., White M., 2016b, *Journal of Cosmology and Astro-Particle Physics*, 2016, 007

Wang L., Reid B., White M., 2013, *MNRAS*, 437, 588–599

Weinberger R., et al., 2017, *MNRAS*, 465, 3291

White M., 2014, *MNRAS*, 439, 3630

Zel'dovich Y. B., 1970, *A&A*, 5, 84

van de Weygaert R., Bertschinger E., 1996, *MNRAS*, 281, 84

APPENDIX A: THE CTM TRAJECTORY CALCULATION

The CTM trajectory is an expansion of the gravitationally induced trajectory around the Zel'dovich approximation, given by

$$\mathbf{x}(\mathbf{q}, t) = \mathbf{q} + A(t) \Psi(\mathbf{q}, t_i) + \epsilon_{\text{CTM}} \int_{t_i}^t \frac{dt'}{a^2} \int_{t_i}^{t'} dt'' \Delta \mathbf{g}(\mathbf{x}(\mathbf{q}, t''), t'') \quad (\text{A1})$$

where a is the scale factor, \mathbf{q} is the initial position, Ψ is the linear order displacement field, t_i is some initial time. The gravitational field is given by $\mathbf{g} = -\nabla_{\mathbf{x}} \phi$ where ϕ is the gravitational potential and ϵ_{CTM} is an expansion parameter used to control the size of the higher-order gravitational term. As the Zel'dovich approximation already extrapolates the effects of the linear gravitational field, we add the differential gravitational field $\Delta \mathbf{g} = \mathbf{g} - \mathbf{g}_{\text{L}}$, where we have removed the linear field to avoid double-counting forces. The CTM trajectory in Equation (A1) then describes a particle moving under free motion given by the Zel'dovich approximation with the addition of a gravitational correction term.

The CTM approach is a hybrid of KFT (Bartelmann et al. 2014a,b, Ali-Haïmoud 2015) and LPT (Moutarde et al. 1991, Catelan 1995, Buchert 1992, Buchert & Ehlers 1993, Bouchet 1996, Tatekawa 2004, Rampf & Buchert 2012). In the KFT approach, the trajectory is based on the formal solution to the particle equations of motion, and so have the free particle motion is damped by the expansion. Here we have chosen to have the trajectory in Equation (A1) to be defined by the Zel'dovich approximation plus a higher-order gravitational term we are free to pick the time-dependent function, $A(t)$, to be the linear growth factor, D_1 , which will allow us to avoid re-normalisation on large scales. In the remainder of this section, we will demonstrate how the second-order CTM trajectory, given in Equation (2) is obtained by solving the gravitational field using the Zel'dovich approximation as a basis. This allows us to avoid the inclusion of non-local terms, which arise when considering second-order LPT.

We can write the trajectory (A1) as

$$\mathbf{x}(\mathbf{q}, t) = \mathbf{q} + \mathbf{x}_0(\mathbf{q}, t) + \mathbf{x}_1(\mathbf{q}, t) \quad (\text{A2})$$

with

$$\mathbf{x}_0(\mathbf{q}, t) = A(t) \Psi(\mathbf{q}, t_i), \quad (\text{A3})$$

$$\mathbf{x}_1(\mathbf{q}, t) = \epsilon_{\text{CTM}} \int_{t_i}^t \frac{dt'}{a^2} \int_{t_i}^{t'} dt'' \Delta \mathbf{g}(\mathbf{x}(\mathbf{q}, t''), t'') \quad (\text{A4})$$

The overdensity field, $\delta(\mathbf{x}, t)$, is given by

$$\delta(\mathbf{x}, t) = \int d^3 q \delta_{\text{D}}(\mathbf{x} - \mathbf{q} - \mathbf{x}_0 - \mathbf{x}_1) - 1 \quad (\text{A5})$$

and its Fourier transform¹ is

$$(2\pi)^3 \delta_{\text{D}}(\mathbf{k}) + \delta(\mathbf{k}, t) = \int d^3 q e^{i\mathbf{k}\cdot\mathbf{q}} e^{i\mathbf{k}\cdot(\mathbf{x}_0+\mathbf{x}_1)}. \quad (\text{A6})$$

Using the Poisson equation, $\nabla^2 \phi = \frac{3}{2} H_0^2 \Omega_m a^{-1} \delta = \frac{3}{2} \omega_0^2 a^{-1} \delta$, with $\omega_0^2 = H_0^2 \Omega_m$ the gravitational field $\mathbf{g}(\mathbf{x}, t)$ can be written as

$$\mathbf{g}(\mathbf{x}, t) = i\omega_0^2 a^{-1} \int \frac{d^3 k}{(2\pi)^3} e^{-i\mathbf{k}\cdot\mathbf{x}} \frac{\mathbf{k}}{k^2} \delta(\mathbf{k}, t) \quad (\text{A7})$$

¹ Our Fourier transform convention is $f(\mathbf{k}) = \int d^3 x e^{i\mathbf{k}\cdot\mathbf{x}} f(\mathbf{x})$ and $f(\mathbf{x}) = \frac{1}{(2\pi)^3} \int d^3 k e^{-i\mathbf{k}\cdot\mathbf{x}} f(\mathbf{k})$.

where $\delta(\mathbf{k}, t)$ is the non-linear overdensity field. The overdensity field is given by the Zel'dovich approximation,

$$\delta(\mathbf{x}, t) = \int d^3 q \delta_{\text{D}}(\mathbf{x} - \mathbf{q} - \mathbf{x}_0) - 1, \quad (\text{A8})$$

and the linear displacement is given by

$$\Psi = \int \frac{d^3 k}{(2\pi)^3} e^{-i\mathbf{k}\cdot\mathbf{x}} \frac{\mathbf{k}}{k^2} \delta^{(0)}(\mathbf{k}, t). \quad (\text{A9})$$

These equations define our Cosmological Trajectories Method.

The Beyond Zel'dovich approximation calculates the gravitational correction to second order in the displacement field. To this order the gravitational field is

$$\mathbf{g} = \omega_0^2 \frac{1}{a} A(t) \left(\Psi - A(t) \left[(\Psi \cdot \nabla) \Psi + \nabla \nabla^{-2} \left(\bar{E}^2 - |\delta^{(0)}|^2 \right) \right] \right), \quad (\text{A10})$$

where $\bar{E}^2 = \bar{E}_{ij} \bar{E}_{ji}$, the tidal tensor is $\bar{E}_{ij} = \nabla_i \nabla_j \nabla^{-2} \delta^{(0)}$ and $\delta^{(0)}$ is the linear overdensity field. The first term in equation (A10) is the linear gravitation field, while the second term represents a local change from Lagrangian to Eulerian coordinates. The last term is the force generated by nonlinear, second-order growth of structure. This term is non-local, depending on all points in the density and tidal field through the inverse Laplacian. However, we can keep our analysis local as we can expect the second term, proportional to the displacement field which we will extrapolate, to be larger than the third term. In addition, we can expect the cancellation between \bar{E}^2 and $|\delta^{(0)}|^2$ in the third terms to reduce its effects. Hence the differential gravitational field, to leading second-order, is

$$\Delta \mathbf{g} \approx -\omega_0^2 \frac{1}{a} A(t)^2 [\Psi(\mathbf{q}, t_i) \cdot \nabla] \Psi(\mathbf{q}, t_i). \quad (\text{A11})$$

Therefore, we define the Beyond Zel'dovich approximation as

$$x_i(\mathbf{q}, t) = q_i + \Psi_i(\mathbf{q}, t_i) \left[A(t) \delta_{ij} + B_\epsilon(t) \bar{E}_{ij}(\mathbf{q}, t_i) \right], \quad (\text{A12})$$

where the tidal term describes the effects of gravitational scattering.

The time-dependent function $B_\epsilon(t)$ is,

$$B_\epsilon(t) = -\epsilon_{\text{CTM}} \omega_0^2 \int_{t_i}^t \frac{dt'}{a^2} \int_{t_i}^{t'} \frac{dt''}{a'} A(t'')^2, \quad (\text{A13})$$

which after using $dt = -\frac{a}{H} dz$ can be written as,

$$B_\epsilon(t) = -\epsilon_{\text{CTM}} \omega_0^2 \int_{z_i}^z \frac{dz'}{a'H(z')} \int_{z_i}^{z'} \frac{dz''}{H(z'')} A(z'')^2. \quad (\text{A14})$$

The Beyond Zel'dovich approximation used in the main body of the paper is the second-order CTM trajectory given in Equation (A12) with the following time-dependent functions

$$A(z) = \frac{D_1(z)}{D_1(z_i)}, \quad (\text{A15})$$

$$B_\epsilon(z) = -\epsilon_{\text{CTM}} \omega_0^2 \int_{z_i}^z \frac{dz'}{a'H(z')} \int_{z_i}^{z'} \frac{dz''}{H(z'')} \left(\frac{D_1(z'')}{D_1(z_i)} \right)^2. \quad (\text{A16})$$

This time dependence reproduces linear growth on large scales without the need for re-normalisation.

APPENDIX B: CORRELATION FUNCTIONS

In Section 2.1.1 we defined the covariance matrix, $\mathbf{C} = \langle \mathbf{X}\mathbf{X}^T \rangle$, where $X_\alpha = (\Psi_i^1, \Psi_i^2, E_i^1, E_i^2, \delta_1^{(0)}, \delta_2^{(0)})$. In order to evaluate the CTM power spectrum it is useful to have the correlation functions defined in Equations (7a, 8a, 8b, 8c, 7b, 7c) re-expressed in of \bar{E}_{ij} . For example,

$$\begin{aligned} \Phi_{ijk}(q) &= \langle E_{ij}(\mathbf{q}_1) \Psi_k(\mathbf{q}_2) \rangle \\ &= \left\langle \left(\bar{E}_{ij}(\mathbf{q}_1) - \frac{1}{3} \delta^{(0)}(\mathbf{q}_1) \right) \Psi_k(\mathbf{q}_2) \right\rangle \\ &= \bar{\Phi}_{ijk}(\mathbf{q}) - \frac{1}{3} \Pi_k(\mathbf{q}) \delta_{ij} \end{aligned} \quad (\text{B1})$$

where

$$\bar{\Phi}_{ijk}(q) = \langle \bar{E}_{ij}(\mathbf{q}_1) \Psi_k(\mathbf{q}_2) \rangle = i \int \frac{d^3 k}{(2\pi)^3} e^{i\mathbf{k}\cdot\mathbf{q}} \frac{k_i k_j k_k}{k^4} P_L(k, z_i), \quad (\text{B2a})$$

$$\Pi_i(q) = \langle \Psi_i(\mathbf{q}_1) \delta^{(0)}(\mathbf{q}_2) \rangle = i \int \frac{d^3 k}{(2\pi)^3} e^{i\mathbf{k}\cdot\mathbf{q}} \frac{k_i}{k^2} P_L(k, z_i), \quad (\text{B2b})$$

with $P_L(k, z_i)$ being the linear power spectrum evaluated at the initial redshift. Similarly,

$$\eta_{ijkl}(q) = \bar{\eta}_{ijkl}(q) + \frac{1}{9} \xi_0(q) \delta_{ij} \delta_{kl} - \frac{1}{3} (\bar{\Sigma}_{ij}(q) \delta_{kl} + \bar{\Sigma}_{kl}(q) \delta_{ij}), \quad (\text{B3})$$

$$\Sigma_{ij}(q) = \bar{\Sigma}_{ij}(q) - \frac{1}{3} \xi_0(q) \delta_{ij}, \quad (\text{B4})$$

with

$$\bar{\eta}_{ijkl}(q) = \langle \bar{E}_{ij}(\mathbf{q}_1) \bar{E}_{kl}(\mathbf{q}_2) \rangle = \int \frac{d^3 k}{(2\pi)^3} e^{i\mathbf{k}\cdot\mathbf{q}} \frac{k_i k_j k_k k_l}{k^4} P_L(k, z_i), \quad (\text{B5a})$$

$$\bar{\Sigma}_{ij}(q) = \langle \bar{E}_{ij}(\mathbf{q}_1) \delta^{(0)}(\mathbf{q}_2) \rangle = \int \frac{d^3 k}{(2\pi)^3} e^{i\mathbf{k}\cdot\mathbf{q}} \frac{k_i k_j}{k^2} P_L(k, z_i), \quad (\text{B5b})$$

$$\xi_0(q) = \langle \delta^{(0)}(\mathbf{q}_1) \delta^{(0)}(\mathbf{q}_2) \rangle = \int \frac{d^3 k}{(2\pi)^3} e^{i\mathbf{k}\cdot\mathbf{q}} P_L(k, z_i). \quad (\text{B5c})$$

B1 An Example of the splitting of a correlation function

We will implement the identities presented in Catelan et al. (2000) and Crittenden et al. (2001) to calculate $\bar{\Sigma}_{ij}$ and Π_i . For example, $\bar{\Sigma}_{ijk}$ given in Equation (B5b) can be written as

$$\bar{\Sigma}_{ij}(q, z_i) = \frac{1}{(2\pi)^2} \int_{-1}^1 d\mu e^{ikq\mu} \int_0^\infty dk k_i k_j P_L(k, z_i) \quad (\text{B6})$$

which after performing the angle integral and substituting in $ik_i = \nabla_i$ results in

$$\bar{\Sigma}_{ij}(q, z_i) = -\frac{1}{2\pi^2} \int_0^\infty dk P_L(k, z_i) \nabla_i \nabla_j j_0(kq). \quad (\text{B7})$$

Defining the following

$$\nabla_i = q_i \frac{d}{dq} = q_i D_q \text{ and } D_r^n j_0(r) = (-1)^n r^{-n} j_n(r) \quad (\text{B8})$$

where $r = kq$ in our case allows us to decompose $\bar{\Sigma}_{ij}$ as

$$\bar{\Sigma}_{ij}(q, z_i) = D(q, z_i) \delta_{ij} + F(q, z_i) \hat{q}_i \hat{q}_j \quad (\text{B9})$$

with $D(q, z_i)$ and $F(q, z_i)$ as defined in Equations (25a) and (25b).

APPENDIX C: COMMENTS ON NUMERICAL INTEGRATION

In Section 3 it is mentioned that we only trust the CTM power spectrum up until $k = 0.9 \text{ h Mpc}^{-1}$. After this point, there are numerical uncertainties due to the highly oscillatory spherical Bessel integrals involved in the calculation. We investigated multiple techniques to remedy these numerical issues for large- k values.

We first implemented an alternative numerical integration technique to the one introduced in Section 2.1.4. This alternate technique was introduced in Vlah et al. (2015a) and involves a generalisation of the plane wave expansion (Mehrem 2011). We will briefly summarise this alternative integration technique here but refer the reader to Vlah et al. (2015a) for a full derivation. The plane wave expansion is

$$e^{i\mathbf{k}\cdot\mathbf{q}} = \sum_{l=0}^{\infty} i^l (2l+1) P_l(\cos \theta) j_l(kr) \quad (\text{C1})$$

using this we can write that

$$(ix)^n = \sum_{l=0}^{\infty} i^l (2l+1) P_l(x) \left(\frac{d^n j_l(\alpha)}{d\alpha^n} \right)_{\alpha=0}. \quad (\text{C2})$$

This is simply the Taylor expansion of the spherical Bessel function around zero. Comparing this Taylor expansion with another well known representation of spherical Bessel function⁶,

$$j_l(\alpha) = \alpha^l \sum_{k=0}^{\infty} \frac{(-1)^k}{2^k k!} \frac{\alpha^{2k}}{(2l+2k+1)!!}, \quad (\text{C3})$$

we can write Equation (C1) as

$$(ix)^n = \sum_{l=0}^{\infty} i^l (2l+1) P_l(x) b_n^l \quad (\text{C4})$$

where

$$b_n^l = \begin{cases} \frac{i^{n-l} n!}{\sqrt{2}^{n-l} \left(\frac{1}{2}(n-l)\right)! (n+l+1)!!}, & \text{if } n \geq l \text{ and } n \text{ and } l \text{ are both even or odd} \\ 0, & \text{otherwise.} \end{cases} \quad (\text{C5})$$

Therefore,

$$\begin{aligned} \int_{-1}^1 d\mu e^{iA\mu} e^{B\mu^2} &= 2 \sum_{n=0}^{\infty} \frac{(2n)!}{2^n n!} B^n \\ &\times \sum_{p=0}^n (-2)^p \frac{4p+1}{(n-p)! (2n+2p+1)!!} j_{2p}(A). \end{aligned} \quad (\text{C6})$$

⁶ <https://dlmf.nist.gov>

In [Vlah et al. \(2015a\)](#) this integration technique was used to calculate both the LPT 1-loop and CLPT power spectra. It was found that there was only a difference between this method and the method used in this paper for high k -values. We also reached the same conclusion in regards to the CTM power spectrum. The method in Section 2.1.4 has numerical advantages as it contains only one infinite sum, hence it was this method that we implemented in the CTM MODULE.

In order to calculate the infinite sum numerically in Equation (31) we truncate the sums at $n = 32$. To reduce the impact of the higher-order spherical Bessel functions on the summation we investigated the impact of truncating the sums at $n = 10$ instead. We found that this removed some of the numerical noise, however, did not impact the maximum k -value reached before we dropped below 5% of the EUCLID EMULATOR.

The spherical Bessel functions in this paper have been calculated using the publicly available MCFIT. This software is based on the FFT-Log algorithm ([Hamilton 2015](#)) and the FFTLOG code ⁷. Although these codes can be fully optimised to calculate the Zel'dovich power spectrum, we encountered issues when the correction term in the CTM trajectory becomes large for either large k -values or low redshifts. We leave it to future work to implement an original integration routine, fully optimised for the CTM power spectrum.

APPENDIX D: APPLICATION OF THE CTM TO KFT

In [Ali-Haïmoud \(2015\)](#) a more detailed computation of the power spectrum to first-order in the gravitational interaction is given. The computation is also described in [Bartelmann et al. \(2014a,b\)](#) from the statistical mechanics perspective. We will simply summarise the results here so that we may compare our power spectrum to that presented in [Bartelmann et al. \(2014a\)](#) and [Bartelmann et al. \(2014b\)](#). Using the definition of the overdensity field (A5) the Dirac delta can be expanded such that

$$1 + \delta^{(0)}(\mathbf{x}) = \int \delta_{\text{D}}(\mathbf{x} - \mathbf{x}_0) d^3q, \quad (\text{D1a})$$

$$\delta^{(1)}(\mathbf{x}) = - \int \mathbf{x}_1(\mathbf{q}) \cdot \nabla \delta_{\text{D}}(\mathbf{x} - \mathbf{x}_0) d^3q. \quad (\text{D1b})$$

To first-order in the gravitational interaction (with $P^{(00)} \propto \langle \delta^{(0)} \delta^{(0)} \rangle$ and $P^{(01)} \propto \langle \delta^{(0)} \delta^{(1)} \rangle$) the power spectrum is given by,

$$P(k) \approx P^{(00)}(k) + 2\epsilon P^{(01)}(k). \quad (\text{D2})$$

It is then noted that \mathbf{x}_0 is equal to the Zel'dovich approximation with the exception of the time dependent function $\alpha(t) = 1 + a_i^2 \frac{\dot{D}_1(t_i)}{D_1(t_i)} \int_{t_i}^t \frac{dt'}{a'^2}$. Therefore, the power spectrum to zeroth order in the interaction is,

$$P^{(00)}(k) = \int d^3q e^{i\mathbf{k} \cdot \mathbf{q}} \left[e^{-k^2 \alpha^2 \sigma_\psi^2 + k_i k_j \alpha^2 \sigma_{ij}(\mathbf{q})} - 1 \right]. \quad (\text{D3})$$

Calculating $P^{(01)}$ is more involved as it requires taking the correlation of $\delta^{(0)}$ and $\delta^{(1)}$. It is calculated in full in [Ali-Haïmoud \(2015\)](#), [Bartelmann et al. \(2014a\)](#) and [Bartelmann et al. \(2014b\)](#). However,

let us focus on the result obtained if one expands in terms of the linear power spectrum

$$P_{\text{L}}^{(00)}(k, z) = \alpha^2(z) P_{\text{L}}(k, z_*), \quad (\text{D4a})$$

$$P_{\text{L}}^{(01)}(k, z) = \omega_0^2 \alpha(z) \int_{t_*}^t \frac{dt'}{a'^2} \int_{t_*}^{t'} \frac{dt''}{a''} \alpha(z'') P_{\text{L}}(k, z_*), \quad (\text{D4b})$$

where $\omega_0^2 = \frac{3}{2} H_0^2 \Omega_m$. There are a number of issues raised in [Ali-Haïmoud \(2015\)](#) concerning the results presented in [Bartelmann et al. \(2014a\)](#) and [Bartelmann et al. \(2014b\)](#). One such issue is with the expansion carried out to calculate the power spectrum. Expanding the Zel'dovich power spectrum in the usual way gives ([Crocco & Scoccimarro 2006a](#))

$$P_{\text{Zel}}(k) \approx P_{\text{L}}(k) - k^2 \sigma_\psi^2 P_{\text{L}}(k) + P_{1\text{-loop}}(k) \quad (\text{D5})$$

with

$$P_{1\text{-loop}}(k) = \frac{1}{2} \int \frac{d^3k'}{(2\pi)^3} \frac{P_{\text{L}}(k') P_{\text{L}}(k'')}{k'^4 k''^4} (\mathbf{k} \cdot \mathbf{k}')^2 (\mathbf{k} \cdot \mathbf{k}'')^2. \quad (\text{D6})$$

where $\mathbf{k}'' = \mathbf{k} - \mathbf{k}'$. The following expansion however, is chosen in [Bartelmann et al. \(2014a\)](#) and [Bartelmann et al. \(2014b\)](#)

$$P_{\text{Zel,B14}}(k) \approx P_{\text{L}}(k) + \frac{P_{1\text{-loop}}}{1 + k^2 \sigma_\psi^2}. \quad (\text{D7})$$

This may lead to enhancement of power on small scales, which is what one would expect from the non-linear power spectrum. Note that there are two free parameters in this approach. There is the time at which the new trajectory is ‘‘switched on’’, z_* and there is the book-keeping parameter, ϵ . In [Ali-Haïmoud \(2015\)](#) z_* is chosen to be $z_* = 99$ and $\epsilon = 1$ to match the results in [Bartelmann et al. \(2014a\)](#) and [Bartelmann et al. \(2014b\)](#).

The second-order CTM time-dependent functions $A(z)$ and $B_\epsilon(z)$ defined in Equation (A14) for KFT are

$$A(z) = \alpha(z) + \epsilon_{\text{CTM}} \omega_0^2 \beta(z), \quad (\text{D8a})$$

$$B_\epsilon(z) = -\epsilon_{\text{CTM}} \omega_0^2 \gamma(z). \quad (\text{D8b})$$

with

$$\alpha(z) = 1 + a_i H(z_i) \frac{D'_1(z_i)}{D_1(z_i)} \int_{z_i}^z \frac{dz'}{a' H(z')}, \quad (\text{D9a})$$

$$\beta(z) = \int_{z_i}^z \frac{dz'}{a' H(z')} \int_{z_i}^{z'} \frac{dz''}{H(z'')} \frac{D_1(z'')}{D_1(z_i)}, \quad (\text{D9b})$$

$$\gamma(z) = \int_{z_i}^z \frac{dz'}{a' H(z')} \int_{z_i}^{z'} \frac{dz''}{H(z'')} \frac{D_1(z'')}{D_1(z_i)} \alpha(z''). \quad (\text{D9c})$$

The difference between the Beyond Zel'dovich approximation (solid lines) and KFT calculated using the CTM (dashed lines) and the emulator is shown in Figure D1 for $z = 0, 1, 2, 3, 4, 5$. Both the Beyond Zel'dovich approximation and KFT were calculated using $\epsilon_{\text{CTM}} = 1$, $z_i = 100$ and $k_c = 6 \text{ h Mpc}^{-1}$. At redshifts, $z = 2$ and above the Beyond Zel'dovich approximation outperforms KFT (calculated

⁷ <https://jila.colorado.edu/~ajsh/FFTLog/>

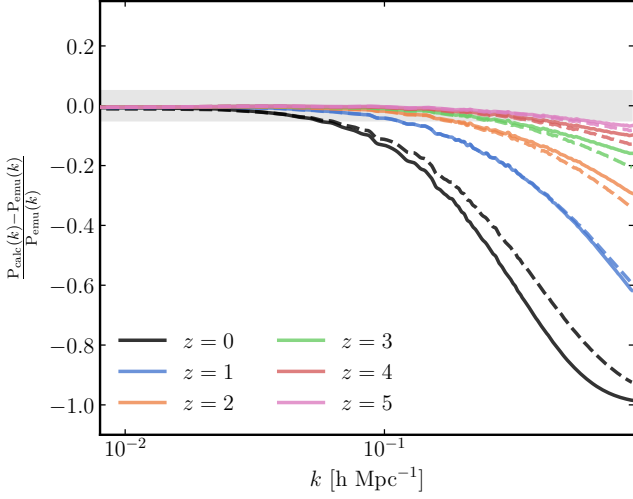


Figure D1. The difference between a given theory and the emulator results is shown for redshifts $z = 0, 1, 2, 3, 4$ and 5 . The difference between the Beyond Zel'dovich approximation and the emulator is shown in solid lines and the differences between KFT and the emulator is shown in dashed lines. The grey shaded region shows $\Delta_{\text{diff}} \pm 0.05$.

using the CTM) when compared to the EUCLID EMULATOR. This is likely due to the time-dependent functions $A(z)$ and $B_\epsilon(z)$ being marginally larger in the Beyond Zel'dovich approximation.

Part of the motivation for the introduction of the CTM and the Beyond Zel'dovich approximation was that KFT does not regain linear growth on large scales as expected. Thus, in Figure D1 the KFT results have been re-normalised by a factor of $A^{-2}(z) \left(\frac{D_1(z_i)}{D_1(z)} \right)^2$.

This paper has been typeset from a $\text{\TeX}/\text{\LaTeX}$ file prepared by the author.